

Combined X-Ray Computed Tomography and X-Ray Fluorescence Drill Core Scanning for 3-D Rock and Ore Characterization: Implications for the Lovisa Stratiform Zn-Pb Deposit and Its Structural Setting, Bergslagen, Sweden

Stefan Luth,^{1,†} Fredrik Sahlström,^{2,3} Mikael Bergqvist,⁴ Alexander Hansson,⁴ Edward P. Lynch,¹ Stefan Sädbom,⁵ Erik Jonsson,^{1,6} Stefan S. Andersson,⁶ and Nikolaos Arvanitidis¹

¹*Department of Mineral Resources, Geological Survey of Sweden, 75128 Uppsala, Sweden*

²*Department of Geosciences, UiT The Arctic University of Norway, 9037 Tromsø, Norway*

³*Geological Engineering Program, Pontificia Universidad Católica del Perú, San Miguel, Lima 32, Peru*

⁴*Orexplore, 164 40 Kista, Sweden*

⁵*Lovisagruvan AB, 711 77 Stråssa, Sweden*

⁶*Department of Earth Sciences, Uppsala University, 75236 Uppsala, Sweden*

Abstract

We present the results of a pilot study that integrates automated drill core scanning technology based on simultaneous X-ray computed tomography (XCT) and X-ray fluorescence (XRF) analyses to provide high-spatial-resolution (<0.2 mm) information on 3-D rock textures and structures, chemical composition, and density. Testing of its applicability for mineral exploration and research was performed by scanning and analyzing 1,500 m of drill core from the Paleoproterozoic Lovisa stratiform Zn-Pb sulfide deposit, which is part of a larger mineral system also including Cu-Co and Fe-(rare earth element) mineralization, hosted by the highly strained West Bergslagen boundary zone in south-central Sweden.

The obtained scanning data complements data derived from structural field mapping, drill core logs, and chemical analysis as well as from multiscale 3-D geologic modeling at Lovisa. Data integration reveals macro- and mesoscopic folding of S_0/S_1 by asymmetric steeply SE-plunging F_2 folds and N-striking vertical F_3 folds. Stretching lineations, measured directly from the scanning imagery, trend parallel to F_2 fold hinges and modeled ore shoots at the nearby Håkansboda Cu-Co and Stråssa and Blanka Fe deposits. The textural character of the Lovisa ore zones is revealed in 3-D by XCT-XRF scanning and highlight remobilization of Zn and Pb from primary layering into ductile and brittle structures. The downhole bulk geochemical trends seen in scanning and traditional assay data are generally comparable but with systematic variations for some elements due to currently unresolved XRF spectral overlaps (e.g., Co and Fe).

The 3-D deformation pattern at Lovisa is explained by D_2 sinistral transpression along the West Bergslagen boundary zone in response to regional north-south crustal shortening at ca. 1.84–1.81 Ga. Local refolding was caused by D_3 regional east-west crustal shortening resulting in dextral transpression along the West Bergslagen boundary zone, presumably at ca. 1.80–1.76 Ga. Based on polyphase ore textures and modeled ore shoots aligned to F_2 fold hinges, we postulate that D_2 and D_3 transpressive deformation exerted both a strong control on ore remobilization and the resulting orebody geometries at Lovisa and neighboring deposits within the West Bergslagen boundary zone.

We conclude that the combined XCT-XRF drill core scanning technique provides a valuable tool for 3-D ore and rock characterization, generating continuous downhole data sets, with the potential for increasing precision and efficiency in mineral exploration and mining.

Introduction

The globally increasing demand for metals requires the development of more time- and cost-efficient methods to collect and synthesize geologic data (e.g., Mudd et al., 2017; Nassar

et al., 2020). In addition, current requirements in mining and exploration to exploit deeper-seated ore deposits and to reduce the environmental impacts of extraction demand integration of multiscale 3-D models based on geologic, geochemical, and geophysical data sets (e.g., Niiranen et al., 2019; Dentith et al., 2020). Key data for the generation of

[†]Corresponding author: e-mail, stefan.luth@sgu.se

such 3-D models include ore and rock structures, textures, mineralogy, geochemistry, and petrophysical properties, most or all of which are primarily derived from drilling (e.g., Wood and Hedenquist, 2019). The subsequent sampling and analyses needed to extract such data from drill cores are typically time-consuming and sample destructive.

During the last decades, several fast and nondestructive techniques for extracting various data from rock samples and drill cores have emerged. In this context, geologic structures in drill core can be measured with the assistance of modern handheld devices, using, for example, laser alignment, although these typically exclude structures that occur within the core, such as lineations and fold hinges (e.g., Kramer-Bernhard et al., 2020). X-ray fluorescence (XRF) and hyperspectral infrared scanning are used to provide 2-D elemental and mineral maps of rock surfaces, respectively (e.g., Kruse et al., 2012; Wiedenbeck, 2013; Sjöqvist et al., 2015; Young et al., 2016; Mathieu et al., 2017; Ryan et al., 2018). X-ray computed tomography (XCT) is another relatively new scanning technique used in geologic applications for 3-D imaging and rock characterization (e.g., Williams et al., 2018). Up until recently, high-resolution XCT studies for mineral exploration have mainly been conducted on gold and platinum group metal ores to characterize their paragenesis and textures, thus contributing to genetic and economic evaluations and to more efficient ore processing (e.g., Godel et al., 2006; Kyle et al., 2008; Godel, 2013; Kyle and Ketcham, 2015). However, despite its potential for ore and rock characterization and the generation of structural data based on 3-D information, XCT is not frequently applied in mineral exploration and especially not for the assessment of long sections of drill core. This is mainly due to the lack of an instrument that can scan several meters of drill core at sufficient speed and resolution and that can also be transported easily to a mine or exploration site (Ketcham, 2005; Cnudde and Boone, 2013; Godel, 2013; Tonai et al., 2019).

Here, we present the results from an experimental study applying a high-resolution drill core scanner that simultaneously combines XCT, XRF, and density analyses to reveal 3-D rock textures, structures, and chemical compositions and their downhole variability. Scanning by the GeoCore X10 instrument was performed both on unoriented and oriented drill core from the actively mined Paleoproterozoic Lovisa stratiform Zn-Pb deposit in Bergslagen, south-central Sweden (Fig. 1). The Lovisa deposit was selected for this pilot study because of its variety of rock types and distinctive ore zones as well as for its complex structural history visible at a range of scales. The obtained results were compared and merged with structural, textural, and chemical data collected by conventional field mapping, drill core logging, and chemical analysis. The merged data sets and interpretations were then used to construct the first multiscale 3-D geologic model of the Lovisa Zn-Pb deposit, also including the nearby Håkansboda Cu-Co and Stråssa and Blanka Fe deposits, thereby providing an integrated 3-D geologic framework for future mineral exploration and new insights into the regional deformation history of the Bergslagen ore province.

Geologic Setting of the Lovisa Zn-Pb Deposit

The Lovisa Zn-Pb sulfide deposit is located in the Bergslagen ore province, south-central Sweden, one of the most diversely

mineralized and extensively mined regions of the Fennoscandian Shield (Fig. 1). Mineralization at Lovisa was interpreted by Jansson et al. (2018) as an originally stratiform syngenetic-exhalative deposit that formed within a continental back-arc basin. The deposit was subsequently deformed and metamorphosed during the ca. 1.9–1.8 Ga Svecofennian orogeny (e.g., Allen et al., 1996; Jansson et al., 2018; Stephens and Jansson, 2020). The deposit consists of two steeply SE-dipping ore horizons; the finely laminated “sphalerite ore” stratigraphically underlies the more massive, sphalerite-galena-bearing “main ore,” both with varying individual thicknesses from 0.1 to 3 m. The two ore horizons are separated by an ~1- to 3-m-wide zone of metamorphosed rhyolitic ash-siltstone, all occurring within a folded and faulted succession of interbedded felsic metavolcanic rocks, banded iron formation, and marble (Fig. 2). The metamorphic grade is characterized by low-pressure and high-temperature amphibolite facies conditions, and the mineralized succession has been affected by both ductile and brittle deformation, resulting in a complex combination of syn- and postgenetic ore textures that provide evidence of extensive sulfide deformation, remobilization, and recrystallization (Jansson et al., 2018; Sahlström et al., 2019a; Jonsson et al., 2020).

Structurally, the Lovisa deposit is located on the western limb of a NE-striking regional fold referred to as the Guldsmedshyttan syncline (Fig. 2; Lundström, 1983; Carlon and Bleeker, 1988; Luth et al., 2019). At Lovisa, this overturned syncline dips steeply to the southeast with a fold axis plunging moderately to steeply to the southwest. At Håkansboda, northeast of Lovisa, the Guldsmedshyttan syncline has been refolded by steeply SE-plunging folds with subvertical NW- to NNW-trending axial planes. The Guldsmedshyttan syncline is part of the larger West Bergslagen boundary zone, an ~150-km-long and 2- to 6-km-wide high-strain deformation zone comprising several NE-striking, steeply dipping shear zones (Fig. 1; Beunk and Kuipers, 2012). Besides the Lovisa and Håkansboda deposits, the West Bergslagen boundary zone hosts various other base metal deposits, of which the Garpenberg Zn-Pb-Ag-(Cu-Au) deposit is the largest by tonnage, and numerous Fe oxide skarn deposits including rare earth element (REE)-rich Bastnäs-type mineralization, such as at Riddarhyttan and Norberg (Fig. 1; e.g., Geijer, 1961; Allen et al., 1996; Sahlström et al., 2019b).

Active mining within the study area occurs only at Lovisa, which comprises a relatively small scale underground operation that yields about 42,000 tonnes/year from a proven and probable reserve of 636,000 tonnes (t) of ore with an average grade of 9.5 wt % Zn and 3.9 wt % Pb (Lovisagruvan AB, 2020). The reserve has been defined by 90 drill holes for 1,100 m along strike and down to 425 m below ground level and is open to the south and at depth.

Methodology

Field mapping, sampling, and litho-geochemistry

Structural data from outcrops were collected in an area within 4 km from the Lovisa Zn-Pb deposit, including also the Håkansboda Cu-Co and Stråssa and Blanka Fe oxide deposits (Fig. 2). Field mapping focused on outcrops located along fold hinges, faults, or geophysical lineaments, as displayed

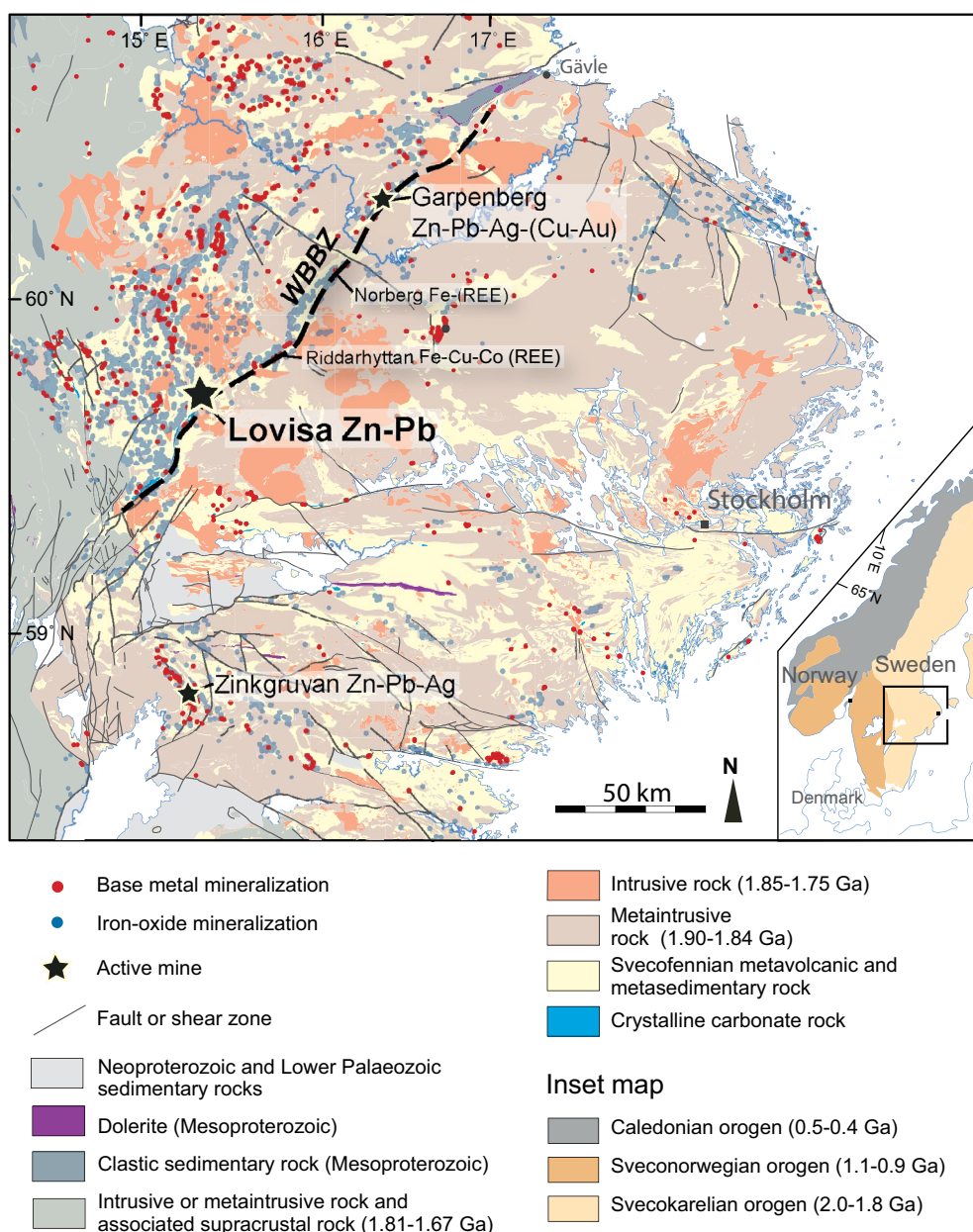


Fig. 1. Geologic map of the Bergslagen region including the locations of active mines and the occurrences of base metal and iron oxide mineralization (modified after Stephens et al., 2009). Data extracted from the mineral resource database of the Geological Survey of Sweden. Dashed line refers to the West Bergslagen boundary zone (WBBZ) as presented in Beunk and Kuipers (2012). Inset figure shows the main tectonic domains in Norway and Sweden.

on available bedrock and mine maps at various scales ranging between 1:50,000 and 1:1,000 (Lundström, 1983; Bleeker, 1984; Carlon and Bleeker, 1988; Jansson et al., 2018) or on magnetic and gravity anomaly maps (Luth et al., 2019). Oriented thin sections were prepared from field-collected rock samples and characterized for microstructures using a polarized-light microscope.

Selected drill core for XCT-XRF scanning comprised 700 m of unoriented full or half core from 10 drill holes (LOV1501–1506 and LOV1802–1805), which collectively transect the Lovisa Zn-Pb ore zones. An additional 800 m of oriented drill core was selected from three exploration drill holes (LOV1901–1903) located between Lovisa and Håkansboda

intersecting marble and metavolcanic rock down to 300 m below the surface.

Whole-rock samples for litho-geochemistry were taken by Lovisagruvan AB from the unoriented drill cores (LOV1501–06) before scanning. Sample lengths varied between 10 and 150 cm, with one sample measuring 3.9 m (see App. 1). The samples were prepared by MS Analytical, Vancouver, Canada, and element concentrations were quantified by inductively coupled plasma-mass spectrometry (ICP-MS) and inductively coupled plasma-atomic emission spectroscopy (ICP-AES) following aqua regia (e.g., Co) or four-acid digestion (e.g., Zn, Pb, Fe₂O₃). For Zn concentrations exceeding 10 wt %, a wet titration technique was used (STI-8Zn). The analytical

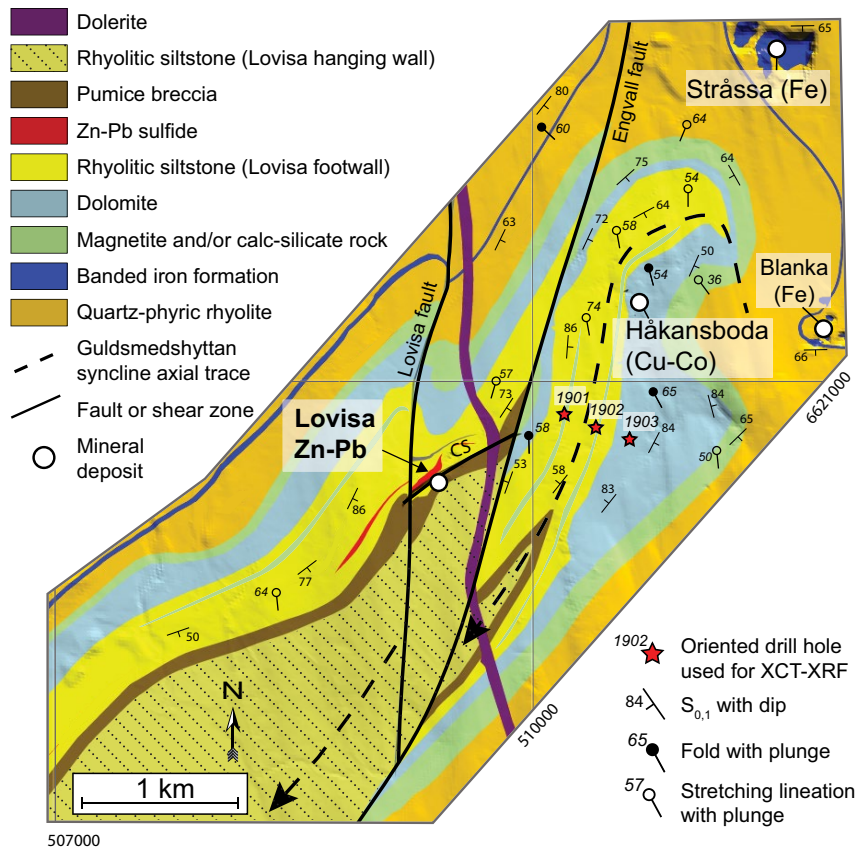


Fig. 2. Geologic map of the study area including the Lovisa Zn-Pb, Håkansboda Cu-Co, and Stråssa and Blanka Fe deposits. Only Lovisa is currently mined. Displayed structural measurements are a selection from the full data set collected for this study (see also Fig. 9). The map, which is largely modified after Jansson et al. (2018), is now synchronized with the 3-D geologic model shown in Figure 10. Map outline corresponds to the width and trend of the West Bergslagen boundary zone (see Fig. 1). All rocks, except the dolerite, are metamorphosed up to amphibolite facies. CS = Central shear. XCT = X-ray computed tomography, XRF = X-ray fluorescence.

precision and accuracy for each applied method is summarized in Appendix 1.

XCT-XRF drill core scanning

Combined XCT-XRF drill core scanning was performed using the transportable GeoCore X10 instrument developed by Orexplore, Stockholm (Fig. 3A; Bergqvist et al., 2019; Orexplore, 2021).

The instrument contains a tungsten solid-anode X-ray source with a 50- μm focal spot size, a transmission detector with a pixel size of 100 μm , and a spectrometer, all moving up and down during scanning while the drill core sections are rotating (spiral scanning). Batches of 4-m-long drill core sections with diameters from 36.65 (BQ) up to 50.5 mm (NQ2) are loaded vertically into the instrument after inserting the individual core pieces into 1-m-long plastic tubes while preserving their relative positions and orientations with respect to the marked core orientation line when present (Fig. 3A). Scanning time may vary between 1 and 6 m/h where low speed results in a higher signal-to-noise ratio. In this study, whole and half drill cores with an initial diameter of 39 mm (WL67) were scanned at rates between 1 and 3 m/h, with an applied X-ray energy of 120 kVp, producing results in 3-D images with a resolution of 200 μm per voxel side.

A precalculated data set of minerals common for Lovisa was used to correlate measured X-ray attenuations to known mineral attenuation values using cross-section data from PENELOPE-2006 (Fig. 3B; App. 2; Salvat et al., 2006). The X-ray imaging system was calibrated using stair-shaped aluminum phantoms, geometric objects used in tomographic imaging to calibrate pixel-to-pixel variations and to correct for beam-hardening effects. The GeoCore X10 utilizes a proprietary technique that combines XRF spectra, attenuation, and density values derived from tomography imaging and sample weight to calculate for mineral compositions and final elemental abundances in weight percent or parts per million (Fig. 2B; Bergqvist et al., 2019). This best-fit approach mitigates analytical challenges associated with heterogeneities in rock samples. Calculations of XRF responses of minerals and tomographic reconstructions were performed on a high-performance computing-class computer equipped with graphics coprocessors (GPUs) capable of teraflop performance.

Detection limits and precision: As with conventional XRF instruments, the detection limits of the GeoCore X10 depend on the applied X-ray energy, scanning rate, bulk composition, density, and particle size distribution of the sample (e.g., Laperche and Lemièrre, 2021). Detection limits for the GeoCore X10 are approximately 100 ppm for elements with

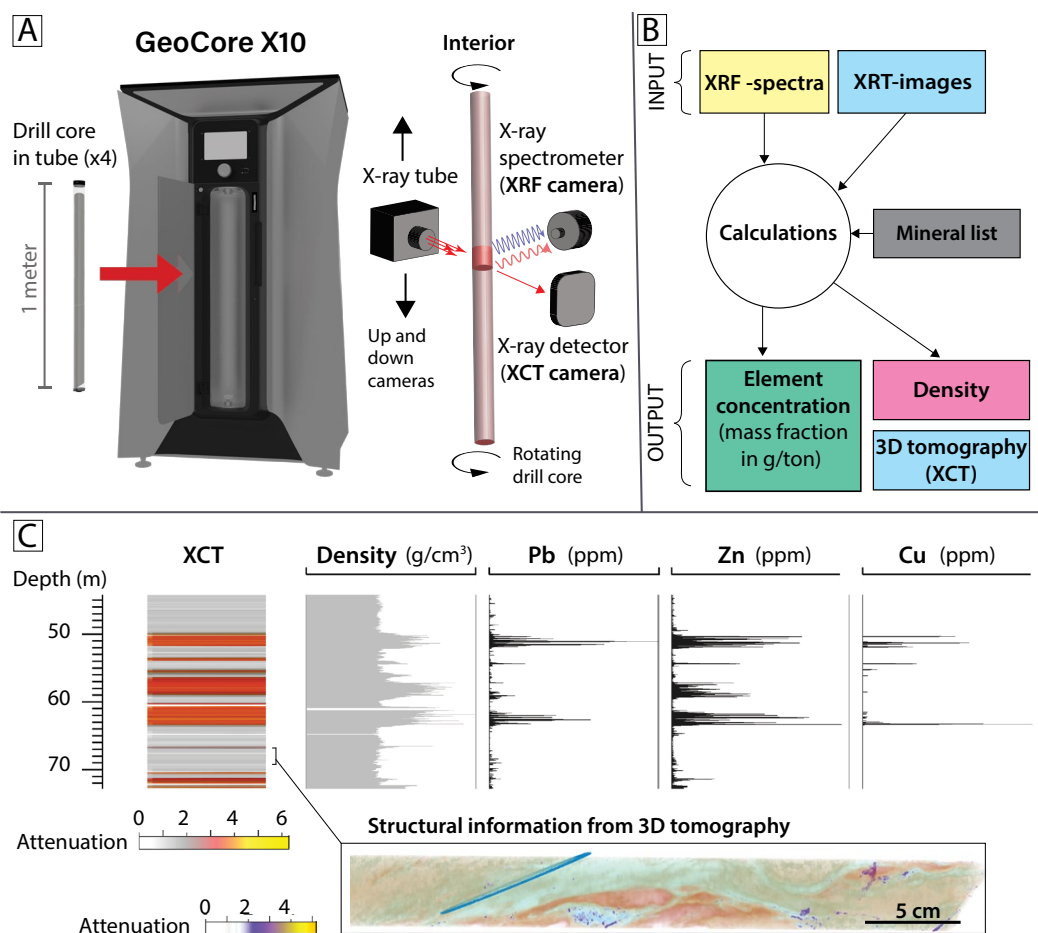


Fig. 3. (A) Illustration of the GeoCore X10 drill core scanner. Core samples are put into 1-m-long tubes of which four can be loaded at the same time into the machine. X-ray transmission (XRT) and X-ray fluorescence (XRF) analysis is undertaken at the same time while applying an X-ray energy up to 130 kVp. (B) Flow chart showing the conversion of X-ray computed tomography (XCT) and XRF-generated data into element concentration and density. The calculations are constrained by the composition of prelisted minerals occurring at Lovisa (see App. 2). (C) Example of a drill log showing XCT attenuation, density, and a selection of elemental concentrations derived from combined XCT-XRF drill core scanning. Visualization and structural measurements on the rotatable 3-D imagery (detailed segment below) were conducted using the Orexplore Insight software.

atomic numbers between 25 and 92. Elements lighter than Cl are not measured but estimated based on stoichiometric calculations, using theoretical half-value layers for XRF spectral lines, which correspond to the material thickness after which the intensity of the radiation has dropped to 50% (App. 3; Salvat et al., 2006). Estimations of the precision of the analyses are derived from repeated measurements on eight drill core samples from various rock and ore types from three different deposits including Lovisa Zn-Pb (see App. 4, Fig. A2). Each core sample measured 1 m in length and was scanned 12 times at a speed of 3 m/h. The obtained standard deviations are relative to the mean value of all 12 measurements and depend strongly on concentration and atomic number of the respective element.

The XCT data from the GeoCore X10 are systematically negatively affected by physical effects such as beam hardening, photon starvation, and scattered radiation (e.g., Joseph and Spital, 1982). Due to these effects, X-rays that pass through massive metallic ore particularly are highly attenuated, obscuring internal rock fabrics by artifacts that cause dark and bright streaks on corresponding images (e.g., Boas and Fleischmann,

2011, and references therein). To partly overcome this, the XCT camera in the GeoCore X10 is a photon-counting cathodoluminescence (CT) type, which offers a higher contrast-to-noise ratio, improved spatial resolution, and optimized spectral imaging (e.g., Willeminck et al., 2018).

3-D visualization and data analysis: The obtained Lovisa scanning data sets were imported into the Orexplore Insight software (Orexplore, 2021), which visualizes the scanned drill core as 3-D, rotatable imagery next to a list of estimated and calculated elemental concentrations. The elemental concentrations were averaged for manually selected segments down to 8 mm in thickness. For oriented drill core (LOV1901-03), the orientation line marked on the core was transposed on the rotatable 3-D imagery, and planar and linear features were observed and measured manually on screen while changing the core viewing angle, rendering, and transparency settings. Survey data (azimuth and dip angle of drilling) were imported for each core to allow for the automatic conversion of structural measurements into true azimuth/trend and dip/plunge values. A brief assessment of the repeatability of the structural measurements on the 3-D tomography is presented in

Appendix 4. The structural data and elemental concentrations were exported as csv files and used for further analysis and 3-D geologic modeling.

3-D geologic modeling

3-D geologic modeling was conducted in three steps, based on scales of the study and used data types. At first, a semiregional 3-D geologic model, measuring $7.5 \times 7.5 \times 2$ km, was constructed using the implicit modeling software Leapfrog Geo v. 6.0, utilizing the geologic maps and profiles presented in Jansson et al. (2018) as well as the new lithological and structural data from this study. Secondly, the Lovisa Zn-Pb ore zones were modeled as a single orebody (ore shell) constrained by underground mapping and 15 drill logs from exploration drilling conducted during the last decade and an additional 75 historical drill logs dating back to the 1980s (e.g., Carlon, 1987; Lovisagruvan AB, 2020). Additional orebody models were constructed for the nearby Håkansboda, Stråssa, and Blanka deposits (Fig. 2) using historical underground mine maps and profiles (Tegengren, 1924; Geijer, 1927; Geijer and Magnusson, 1944; Koark, 1960; Carlon, 1986). The resulting 3-D orebody models were integrated with the semiregional model and their geologic context interpreted. Thirdly, XCT-XRF scanning data was utilized to refine local and regional modeled lithological volumes by adding textural, chemical, and structural constraints from the Lovisa drill cores and from the oriented cores drilled north of the Lovisa mine.

Results

Structures in outcrops and thin sections

The main structures observed in outcrops around Lovisa are S_0 and S_1 planar fabrics that are generally parallel ($S_{0,1}$), asymmetric folds, stretching and intersection lineations, C-S shear fabrics, boudinage, and brittle faults and fractures (Figs. 4, 5). Planar and linear grain-shape fabrics are well developed in mica-rich metavolcanic rocks forming SL tectonites (Fig. 5), whereas marble- and quartz-rich metamorphosed volcanic and intrusive rocks were deformed into L tectonites with lineations plunging steeply to the southeast (Fig. 4A). The bulk of the observed mesoscopic folds have subvertical N- to NE-striking axial planes and are interpreted as F_2 shear folds that are parasitic to the Guldsmedshyttan syncline with predominantly Z asymmetry on its northern limb and S asymmetry on its southern limb (Fig. 4B). Many F_2 folds show isolated fold hinges and strongly vertically and horizontally stretched fold limbs without the development of an axial planar cleavage (Fig. 4B). In contrast, vertical NW-striking folds (F_3) locally re-fold the F_2 folds in outcrop (Fig. 4C) and are portrayed on the map as the hook-like structure in the Håkansboda area (Fig. 2; Carlon and Bleeker, 1988). These younger F_3 folds are associated with a spaced vertical axial planar cleavage striking northwest along which both minor dextral and sinistral displacements were observed (Figs. 4C, F, 5D-F). Southwest of the Lovisa deposit, subvertical F_2 shear folds with variable amplitudes and wavelengths are developed within a well-layered sequence that is located stratigraphically in the hanging wall of the Lovisa deposit (Fig. 4D-F). Here, local refolding of asymmetric N-striking vertical folds (F_{2a}) resulted in folds with similar asymmetry and orientation (F_{2b}), suggesting that

deformation was progressive (Fig. 4D, E). In addition, steeply S- to SE-plunging F_2 sheath and oblique folds with hinges oriented parallel to a penetrative L_2 stretching lineation further reinforce the interpretation that mesoscopic F_2 folding resulted from noncoaxial subvertical shearing (Fig. 4D). Ductile kinematic indicators, such as sigmoids, rotated clasts, and intrafolial folds, observed parallel to the penetrative stretching lineations all imply a reverse, southeast-side-up sense of shear with a sinistral horizontal component (Fig. 5B, C).

Oriented structures from XCT-XRF

From the 3-D tomographic images (XCT) of the oriented drill cores, a large number of fabrics and kinematic indicators were identified and measured, including penetrative linear and planar fabrics, deformed clasts and mineral blasts, folds, and C-S fabrics, as well as fractures and veins (Fig. 6; App. 5). Structures were observed in all drilled lithologies, but the most useful examples are from metavolcanic rhyolitic silt/sandstone and calc-silicate (skarn) rocks in which compositional banding caused clear contrasts in spectral attenuation.

Within the rhyolitic silt/sandstones, the compositional banding is portrayed by slightly different attenuation values, where the lower values correspond to higher quartz contents (Fig. 6A). Whether this banding represents primary bedding/laminae (S_0) or is caused by subsequent deformation (S_1) is not directly evident from the tomography. A linear fabric is defined by elongated and aligned feldspar and mica grains that exhibit higher attenuation than quartz and represent an L_2 stretching lineation (Fig. 6A) or a mineral lineation (Fig. 6B). The lineations are oriented parallel to the compositional banding (Fig. 6A) or locally at moderate angles to it (Fig. 6B). When viewed normal to the lineation, the sigmoidal shape of some distinctive high-attenuation grains/clasts indicates reverse shearing. A reverse sense of shear with top-to-the-northwest movement is also inferred from C-S fabrics with moderately dipping C surfaces containing elongated high-attenuation grains/clasts and steeply dipping S surfaces in which the high-attenuation grains/clasts appear less elongated (Fig. 6C).

Various folds become visible while rotating the tomographic core images in 3-D (Fig. 6D-G). Most folds are Z and S asymmetric and are only visible when viewed normal to the L_2 stretching lineation and parallel to the axial plane (Fig. 6D). These folds appear to fold earlier-formed planar and linear fabrics and are interpreted as F_2 oblique or shear folds that formed by reverse ductile shearing with top-to-the-northwest movement, which is consistent with kinematic indicators observed in outcrops (see previous section). F_3 folds fold the planar ($S_{0,1}$) and linear fabrics, which was observed on the XCT image when viewed both normal and parallel to the L_2 stretching lineation (Fig. 6E-G). The F_3 folds are typically associated with fractures and veinlets oriented parallel to the fold axial planes. The bulk of the observed fractures and veins, however, are not associated with folding and clearly overprint the ductile fabric (Fig. 6H, I). Fractures with a fracture fill other than quartz show mostly high attenuation and are easily recognized in the tomographic images (Fig. 6H), whereas fractures filled with quartz or having no fill are determined indirectly from a disrupted preexisting fabric. In a few cases, a displacement vector could be measured by restoring dislocated and distinctive lithoclasts along a fracture plane (Fig. 6I).

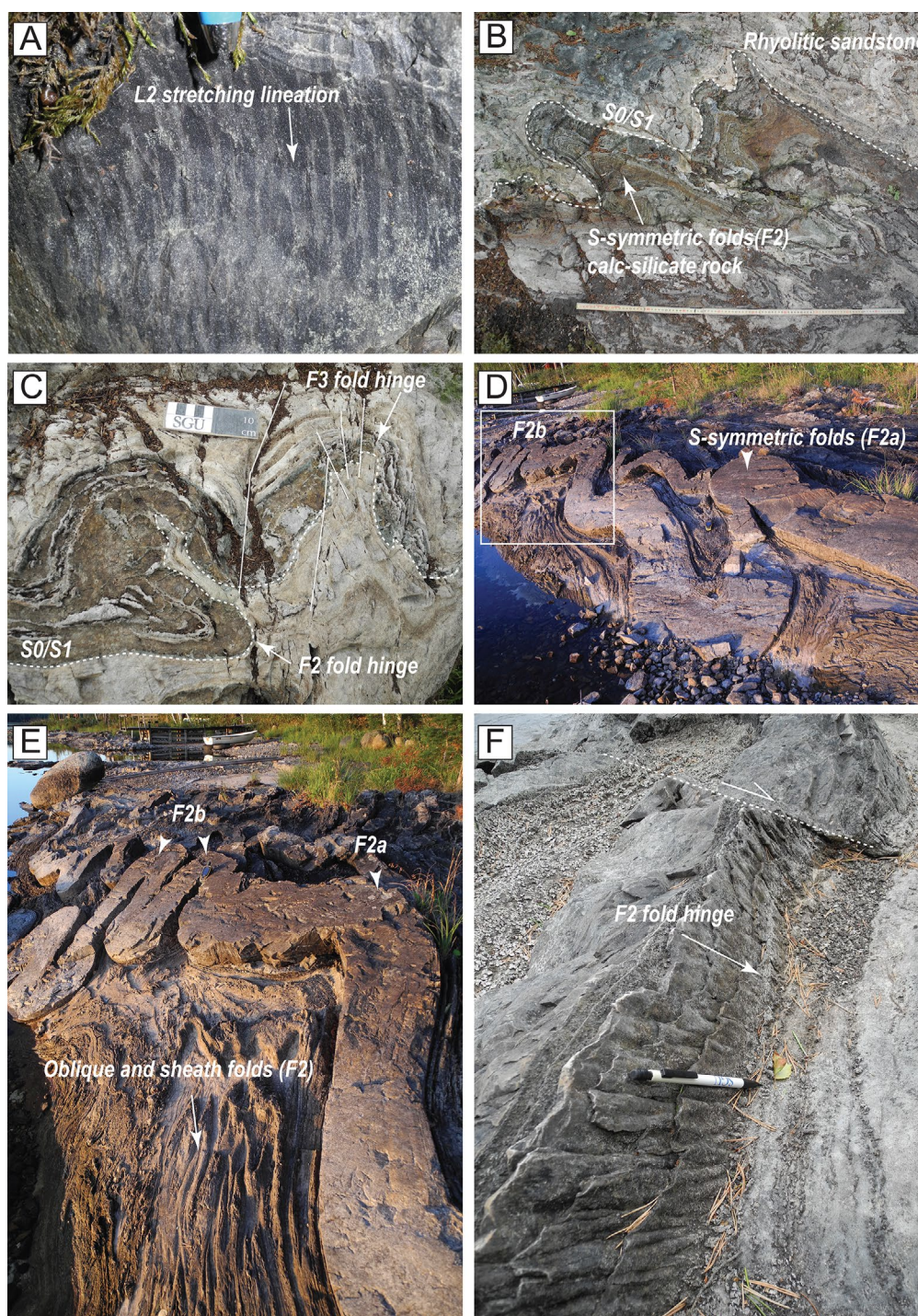


Fig. 4. Character of structures in outcrops near the Lovisa Zn-Pb deposit. (A) Stretching lineations (L_2) developed in a metamorphosed rhyolitic sandstone plunging steeply toward the southeast at Håkansboda. View to the southeast. Width of the picture is approximately 5 cm. (B) Local asymmetric folding (S-type) of a layer of calc-silicate rock within metamorphosed rhyolitic sandstone located northeast of the Lovisa mine. The fold asymmetry indicates a sinistral vergence. View to the northwest on the top surface. (C) Local F_3 folds affecting the long limb of the F_2 fold by refolding the same calc-silicate layer as shown in (B). View to the northwest on the top surface. (D) S-symmetric folding of thick (meta-)rhyolitic sandstone layers standing out from a sequence of strongly folded beds of alternating rhyolitic sandstone and siltstone. Local refolding of the F_{2a} long limbs (by long-wavelength F_{2b} folds) and short limbs (by short-wavelength F_{2b} folds) resulted from progressive deformation rather than from a separate deformation phase. Location is at Lake Usken south of the Lovisa mine. White box outlines view shown in (E). View to the east. (E) Detailed view of (D) showing multiple M folds located on the short limb of the larger S-folded rhyolitic sandstone layer. Folds of the thinner beds (lower part of image) show much shorter wavelength and are locally developed into sheath folds. View to the northeast. (F) Detailed view south of (E) showing steeply plunging folds of mainly thinner beds. A NW-striking fault shows dextral displacement of a (meta-)rhyolitic sandstone layer. View is toward south.

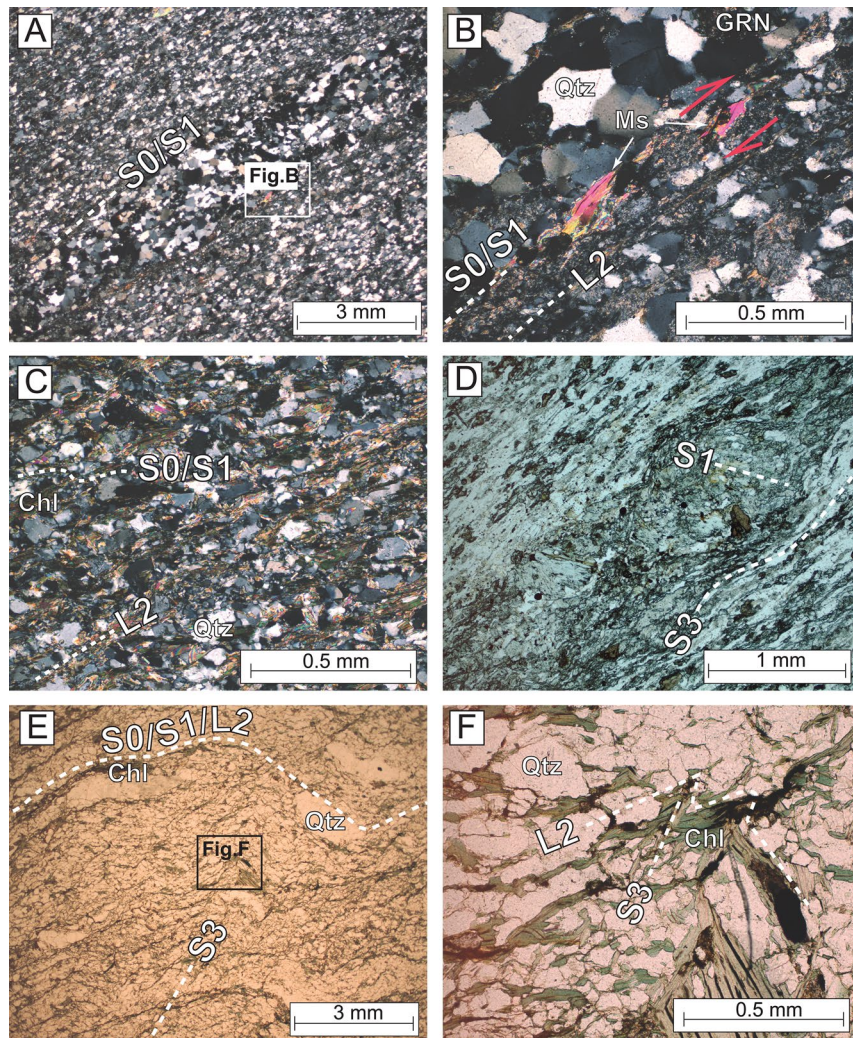


Fig. 5. Character of microstructures near the Lovisa mine as observed in thin sections. (A) A metamorphosed rhyolitic sandstone of predominantly quartz with minor biotite and muscovite. A compositional banding (S_0) is evident from the variable mica content and grain size and is paralleled by a tectonic fabric (S_1). Cross-polarized light. Section oriented parallel to stretching lineation (L_2). (B) Detailed view of (A) highlighting quartz-rich Q domains (upper left) with garnet and annealed recrystallized quartz and micaceous P domains (lower right) containing mica fish indicating top-to-the-right (reverse) sense of shear along L_2 . (C) Metamorphosed rhyolitic sandstone with quartz-mica fabric ($S_{0,1}$) crenulated and overprinted by reverse shearing along L_2 composed of biotite, white mica, and chlorite. Cross-polarized light. Section oriented parallel to stretching lineation (L_2). (D) Mica-quartz mylonite with a S_3 mylonitic fabric wrapping around recrystallized blasts that contain a pre- D_3 fabric. Plane-polarized light. Section oriented horizontally with top to the east. (E) Rhyolitic sandstone composed of quartz-rich layers alternating with chlorite and biotite layers representing $S_{0,1}$ and L_2 . The layers are intersected by S_3 cleavages oriented parallel to the fold-axial planes (F_3). Plane-polarized light. Section oriented horizontally with top to the south-southwest. (F) Detailed view of (E) showing chlorite that replaced biotite within the hinge zone of an F_3 kink fold. Plane-polarized light. Section oriented horizontally with top to the south-southwest. Abbreviations: Chl = chlorite, GRN = garnet, Ms = muscovite, Qtz = quartz.

Ore textures and chemistry from XCT-XRF

Three examples of representative ore textures and associated XCT-XRF scanning data, obtained from a 20-m-long drilled section through the Lovisa Zn-Pb orebody, are shown in Figure 7. At the top of the section, the main ore is characterized by a distinctive ball ore texture (e.g., Geijer, 1971; Vokes, 1973), comprising variably sized silicate-rich fragments that occur within a deformed and recrystallized matrix dominated by fine-grained sphalerite and galena (Fig. 7B). The texture reflects folding (F_2 and F_3) of the metavolcanic host rock,

followed by progressive breakup, rotation, and kneading of mostly competent host-rock fragments within a ductile sulfide matrix (e.g., Vokes, 1969, 1973; Fig. 7B). Corresponding concentrations and 3-D distribution of Pb and Zn suggest locally variable degrees of remobilization of sphalerite and galena in the ball ore, with galena preferentially occurring in fold hinges and along contacts with the adjacent metavolcanic rock (Fig. 7C).

Directly below the main ore, networks of veins and fracture fillings consisting of remobilized sulfides cross-cut a laminated metavolcanic rock (Fig. 7E). Two sets of

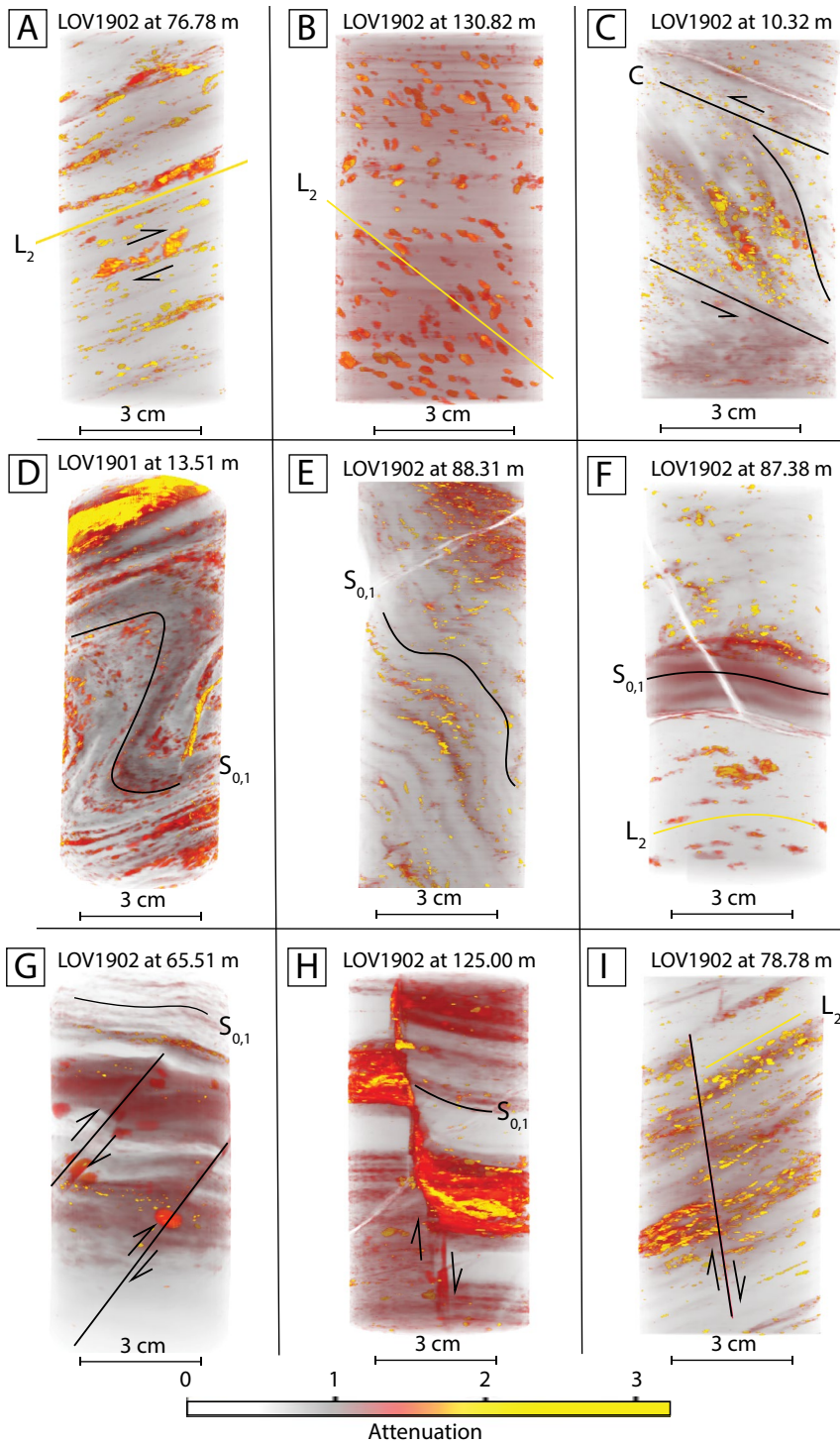


Fig. 6. Tomography images of the X-ray computed tomography and X-ray fluorescence (XCT-XRF) scans on a selection of oriented drill cores (19 series) showing the character of ductile and brittle structures north of the Lovisa Zn-Pb deposit in 3-D. Rotating 3-D views of the scanned segments are included as movie files in Appendix 5. (A) Linear fabric defined by grains with relatively high attenuation (mica and feldspar) in a metamorphosed rhyolitic siltstone. Parallel to the L_2 lineation, an $S_{0,1}$ compositional banding is inferred from the different shades of gray in which the lightest gray corresponds to higher quartz content. Mineral lineation plunges toward the lower left. The sigmoidal-shaped fragments below the center of the image indicate top-to-the-right (northwest) movement. View is normal to lineation. (B) Linear fabric defined by the alignment of slightly elongated feldspar clasts with relatively high attenuation within a rhyolitic sandstone. The L_2 linear fabric plunges toward the lower right (southeast) at a 45° angle to the compositional banding (grayish colors). View is normal to lineation. (C) Composite CS fabric in the center of the image indicating top-to-the-left (northwest) movement in sillimanite-bearing metamorphosed rhyolitic sandstone. S and C surfaces dip steeply and moderately to the lower right, respectively. View is normal to CS fabric. (D) Z-asymmetric F_2 fold affecting compositional banding in magnetite-rich calc-silicate rock (skarn). Folding is revealed only when viewing parallel to the stretching lineation. View is parallel to fold axis and mineral lineation. (E) Moderately inclined F_3 fold that folds compositional banding in metamorphosed rhyolitic siltstone. This folding is probably low temperature and associated with faulting as inferred from the fault with similar vergence in the upper part of the image. View is normal to compositional banding. (F) Gentle upright F_3 folding of compositional banding and a lineated fabric in metamorphosed rhyolitic siltstone. Quartz veins occur both parallel and at an angle to the compositional banding and postdate folding. View is normal to compositional banding. (G) Asymmetrical F_3 folding of compositional banding associated with reverse faulting in garnet-pyroxene-bearing calc-silicate rock (skarn). View is normal to compositional banding. (H) Normal faulting and drag folding of metamorphosed rhyolitic sandstone containing magnetite-rich skarn interbeds (red and yellow). Normal fault is subvertical and is partly filled with skarn minerals. View is normal to compositional banding. (I) Normal faulting of lineated fabric in metamorphosed rhyolitic siltstone. The fault is subvertical and was only interpreted by the 3-D offset of the lineated fabric. View is normal to lineation.

sulfide-bearing veins and fractures are present, oriented subparallel to primary layering and oriented at high angles to primary layering, respectively. The combined XRF and XCT scan data reveal a transition from $Pb > Zn$ to $Zn > Pb$ from top to bottom of the sample, indicating variable proportions of galena and sphalerite (Fig. 7G). A few meters downhole, the sphalerite ore preserves what has been interpreted as folded (F_2 and F_3) syndepositional layering ($S_{0,1}$) of fine-grained sulfides (sphalerite with minor intergrown galena

and pyrite) alternating with (meta-)rhyolitic interbeds (Fig. 7H; Jansson et al., 2018; Sahlström et al., 2019a). Locally, sulfide-rich veins or fracture fillings protrude from the fold hinges. Unlike in hand specimen (Fig. 7H), the thin sulfide layers can be readily distinguished from rhyolitic interbeds in the XCT scan, thereby enhancing visualization of delicate pinching-out and folding structures (Fig. 7I). Overall, galena was extensively remobilized from the preexisting layering into veins parallel to fold hinges during ductile deformation,

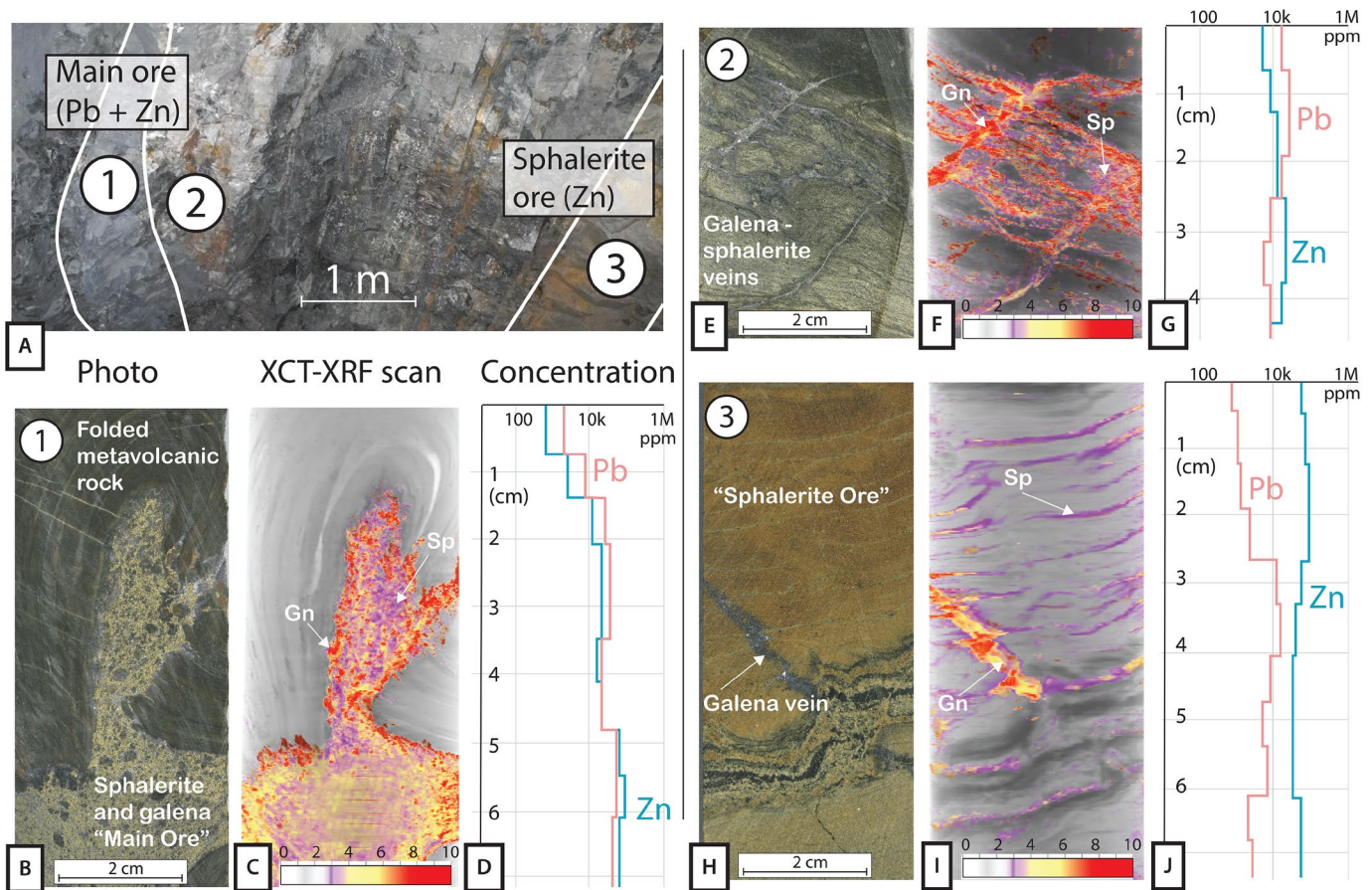


Fig. 7. (A) Locations of three drill core samples representing different ore types projected on an underground rock face within the Lovisa Zn-Pb mine viewed to the south. Sample 1 represents the main ore and is derived from drill hole LOV1503 at 176.7 m, sample 2 galena-sphalerite veins in metavolcanic rhyolitic rock from LOV1505 at 147.8 m, and sample 3 sphalerite ore from LOV1502 at 153.4 m. The samples are shown as photos (B, E, H), X-ray computed tomography and X-ray fluorescence (XCT-XRF) scanning images with coloring corresponding to X-ray attenuation (C, F, I), and associated element plots for lead and zinc (D, G, J, note log scale). Gn = galena, Sp = sphalerite, which can be distinguished on the scan images by lower attenuation for Zn (yellow) and higher attenuation for Pb (red). Notice the different color scale applied to the XCT-XRF images compared to Figure 6 to enhance color contrast between ore minerals. Rotating 3-D views of the scanned segments are included as movie files in Appendix 5.

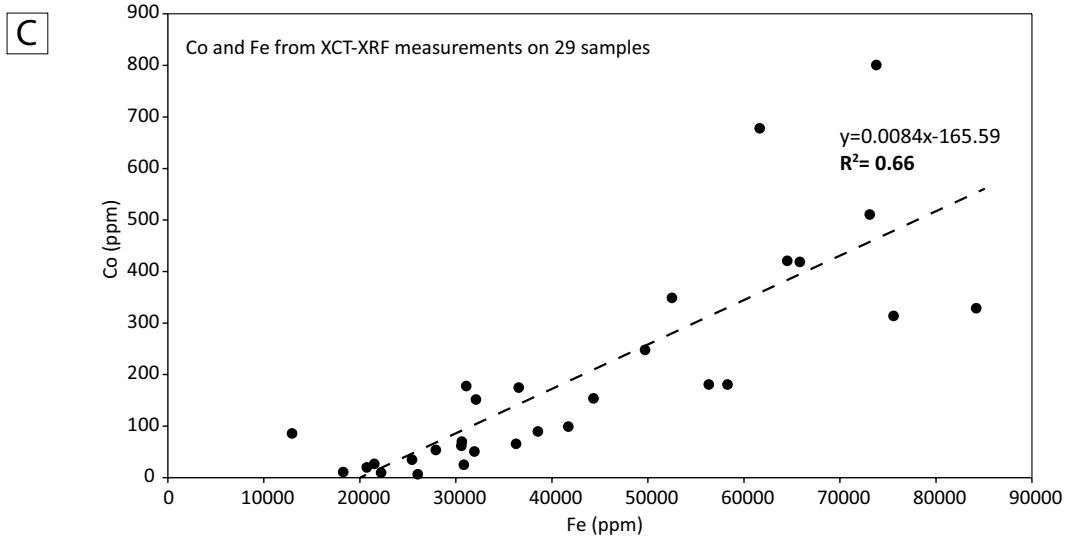
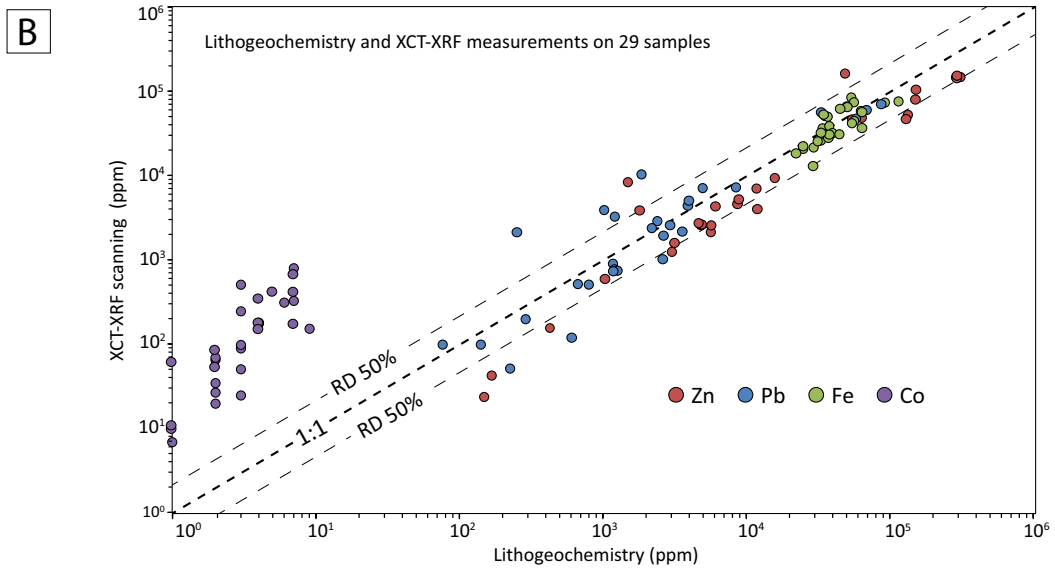
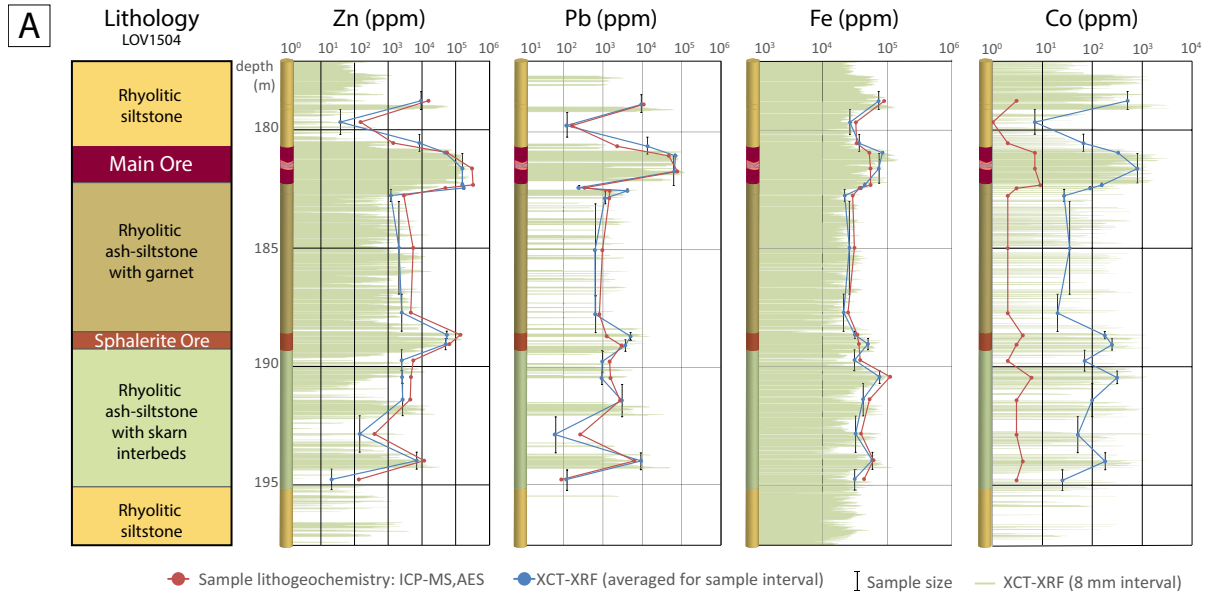
while sphalerite largely remained within the layering. This differential sulfide remobilization has caused significant centimeter-scale variability in Zn (0.5–9%) and Pb grades (0.1–3%; Fig. 8J).

Comparison between XCT-XRF and litho geochemistry

The obtained concentrations of Zn, Pb, Fe, and Co from XCT-XRF scanning have been compared with the results from 18 litho geochemistry samples from a 20-m, ore-bearing drill

core section (Fig. 8A, B; App. 1). The concentrations derived from XCT-XRF scanning were averaged over the same length intervals as the samples used for litho geochemistry analysis. Additionally, XCT-XRF data for 8-mm-thick intervals, the minimum selectable thickness of core segments in Insight, were included in the comparison (Fig. 8A). Note that scanning was conducted after sampling for litho geochemistry analysis, meaning that the comparison is based on two analyses of different material derived from opposing pieces of half core.

Fig. 8. (A) Lithological column of drill hole LOV1504 intersecting the Lovisa Zn-Pb ore zones and surrounding host rocks. All rocks are metamorphosed up to amphibolite facies (see Fig. 11 for drill location). Element logs for Zn, Pb, Fe, and Co are shown to the right and are based on the results from litho geochemistry analysis on 18 half-core samples (red dots are mid-points) and from X-ray computed tomography and X-ray fluorescence (XCT-XRF) scanning of the remaining half-core corresponding to the same sampling intervals (blue dots are midpoints) and 8-mm intervals (green bars). (B) Comparison of Zn, Pb, Fe, and Co concentrations obtained from litho geochemistry analysis and XCT-XRF scanning of 29 half-core samples from drill holes LOV1503–04. Dashed line represents a 1:1 correlation corresponding to 0% relative difference (RD) between the results of both analytical methods. (C) Correlation plot of Co and Fe concentrations obtained from XCT-XRF scanning of 29 half-core samples from LOV1503–04. R^2 refers to squared correlation coefficient between Co and Fe concentrations. (See text for explanation.) ICP-AES = inductively coupled plasma-atomic emission spectroscopy, ICP-MS = inductively coupled plasma-mass spectrometry.



The resulting downhole logs (Fig. 8A) reveal broadly similar compositional trends with elevated concentrations of Zn, Pb, Fe, and Co in the main ore and sphalerite ore. A correlation plot for XCT-XRF scanning and litho-geochemistry data from 29 samples (Fig. 8B) shows significant variation for Zn (avg relative difference ~50%), whereas Pb and Fe reveal less variation (avg relative difference of ~37 and 21%, respectively). Due to analysis of opposing core pieces, this variation may be both geologic and analytical. No correlation exists between variation and sample core length. For Co, despite an overall similar relative compositional trend (Fig. 8A), concentrations from XCT-XRF scanning are one to two orders of magnitude higher than those obtained from litho-geochemistry analysis on whole-rock samples (Fig. 8B). This systematic overestimation by XCT-XRF for Co is likely due to overlap between emission lines Co-K α and Fe-K β (e.g., Potts and Webb, 1992), which is also supported by the observation that both elements follow the same general trend within the succession (Fig. 8A, C). Such a spectral interference between Co and Fe has also been noted in portable XRF analysis (e.g., Gallhofer and Lottermosser,

2018). Highly localized variations for all displayed elements are suggested by the XCT-XRF 8-mm interval plots (Fig. 8A). For example, locally elevated concentrations of Pb (at 192 and 194 m) and Zn (at 178 and 192 m) are missed by the sampled interval plots and can be explained by very localized concentrations of galena or sphalerite, respectively.

Comparison between structural trends

Structural measurements from outcrop were plotted in stereonet to determine regional trends and for a comparison with orientations interpreted from 3-D tomographic imagery (XCT) of oriented drill cores (Fig. 9). From outcrop measurements, poles to the $S_{0,1}$ planes plot along a great circle, reflecting regional-scale F_2 folding around a steeply plunging, SE-trending fold axis (Fig. 9A). The fold hinges of mesoscopic F_2 and F_3 folds in outcrop plunge between 45° and 85° to the south and southeast (Fig. 9B). Likewise, the bulk of the L_2 stretching lineations plunge between 40° and 75° to the south-southeast. Some folds and lineations, however, trend toward the east-northeast, which combined in stereonet give rise to a regional doubly plunging fold with an axial

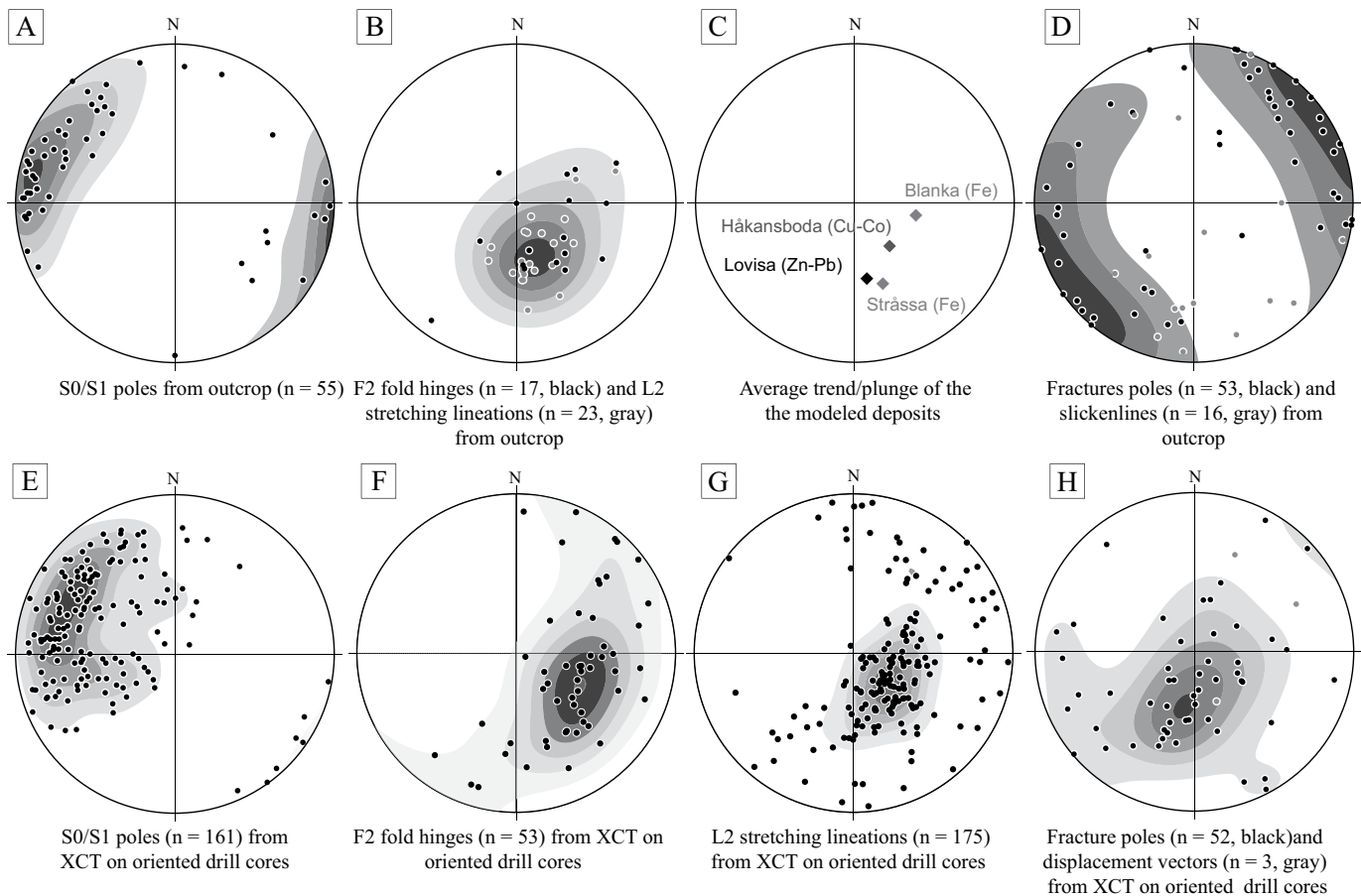


Fig. 9. Lower-hemisphere, equal-area stereonet projections of geologic structures. (A, B, D) Structures measured in outcrops located around the Lovisa and Håkansboda deposits (Fig. 2). (C) Overall orientation of the ore deposits occurring within the study area (Fig. 10). (E-H) Structures measured from 3-D tomography (X-ray computed tomography; XCT) on oriented drill core from three exploration drill holes (LOV1901–1903). Compositional banding ($S_{0,1}$) and fractures are plotted as poles from planes. Fold hinges, lineations, and slickenlines are plotted as lines. Contouring of data is at a 3σ significance level using Exponential Kamb from the method of Kamb (1959). Slickenlines (D) and displacement vectors (H) were excluded from contouring. Displacement vectors are plotted as lines and were interpreted in 3-D from clearly displaced features such as a layer or mineral.

planar surface dipping $\sim 50^\circ$ to the east-southeast. Furthermore, brittle structures including fractures, spaced cleavages, and faults (Fig. 9D) are predominantly dipping between 75° and 90° toward the northeast and southwest. The bulk of the slickenlines on fractures, cleavages, and fault surfaces plunge between 5° and 30° toward the southeast and are consistent with sinistral movements.

The 3-D models of the Håkansboda Cu-Co and Blanka Fe deposits reveal rod-shaped orebodies that plunge between 50° and 60° to the southeast and east, respectively (Figs. 9C, 10). Similarly, the dominant folds of the modeled Lovisa Zn-Pb and Stråssa Fe deposits plunge steeply ($\sim 55^\circ$) to the south-southeast. Hence, the modeled ore shoots and folds have orientations comparable to those of the F_2 fold hinges and stretching lineations measured in outcrops (Fig. 9B, C).

From the XCT imagery, the orientations of the compositional banding in the (meta-)rhyolitic silt/sandstone are comparable to the orientation of the $S_{0,1}$ planes measured in outcrop, and their clustering reflects folding of $S_{0,1}$ around a steeply SE-plunging F_2 fold axis (Fig. 9E). The orientations of F_2 fold hinges and L_2 stretching lineations in the scan are clustered around 60° to the east-southeast (Fig. 9F, G), which is comparable with measurements in outcrop,

albeit the scanning data shows a wider spread toward more gently plunging and NE-trending fold hinges and stretching lineations. Fracture orientations derived from XCT dip between 10° and 60° and therefore differ from the overall steeply dipping planes measured in outcrop (Fig. 9G, H). This contrast may be due to a sampling bias underlain by the underrepresentation of vertical sections in most outcrops as well as by the direction of drilling (perpendicular to $S_{0,1}$). Apart from varying dips ranging between 0° and 90° a general northwest-southeast strike of fractures is apparent from both data sets.

3-D geologic modeling using XCT-XRF-generated data

The structural and geochemical data derived from XCT-XRF drill core scanning were used to constrain and refine the 3-D geologic model at Lovisa (Fig. 11). The scanned oriented drill cores do not intersect the Zn-Pb ore but do provide valuable geologic constraints along a 2-km NW-SE-oriented section between the Lovisa (Zn-Pb) and Håkansboda (Cu-Co) deposits (Fig. 11A). Firstly, distinctive Fe-rich skarn layers occurring within the metarhyolitic silt/sandstones identified by XCT-XRF and conventional logging were used as stratigraphic marker horizons to correlate the drill cores. The

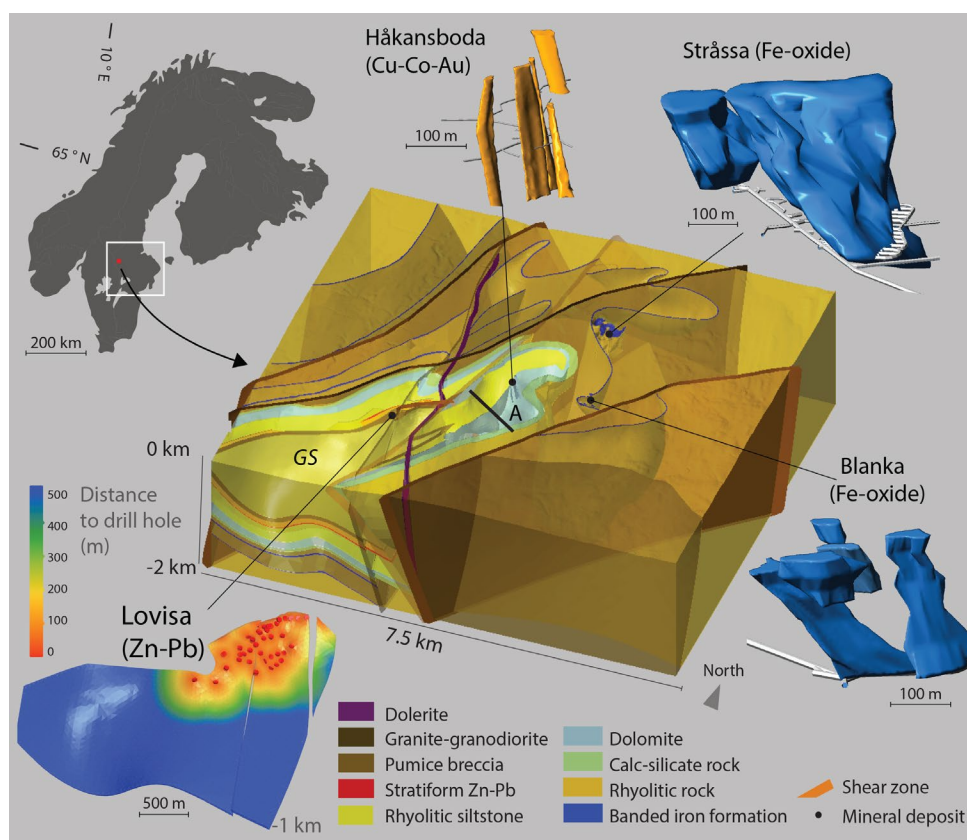


Fig. 10. Semiregional 3-D geologic model including the orebodies of the Lovisa Zn-Pb, Håkansboda Cu-Co, and Stråssa and Blanka Fe deposits based on drilling and mine maps. Orebody surfaces represent geologic contacts and not ore grade. Coloring of Lovisa Zn-Pb orebody indicates distance to drill hole (red dots). The extent of the Lovisa Zn-Pb orebody beyond the depth of drilling (~ 400 m below ground level) is highly uncertain and solely confined by the interpreted regional folding pattern. Inset map of Sweden, Norway, and Finland shows the study area in red within the Bergslagen ore province (white rectangle, Fig. 3). A = section in Figure 11, GS = Guldsmédshyttan syncline. All rocks, except the dolerite, are metamorphosed to amphibolite facies grade. The unit “pumice breccia” is defined in Jansson et al. (2018) and refers to a lithoclast-bearing rhyolitic metavolcanic rock.

resulting pattern outlines an overturned, SE-dipping syncline (Fig. 11B), the Guldsmedshyttan syncline, and is consistent with earlier interpretations based on lithology and way-up indicators from outcrop observations by Carlon and Bleeker

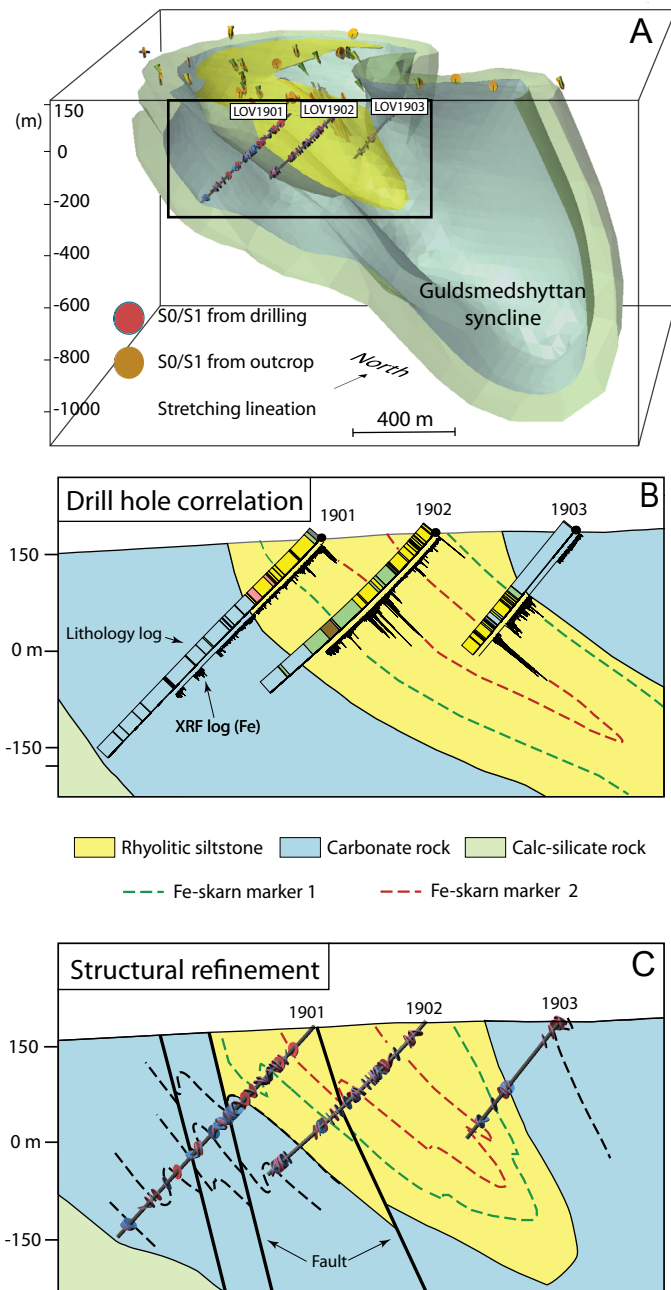


Fig. 11. Local refinement of the geologic model between the Lovisa (Zn-Pb) and Håkansboda (Cu-Co) deposits by using geochemical and structural information from X-ray computed tomography and X-ray fluorescence (XCT-XRF) scanning on three oriented drill cores. (A) Regional 3-D geologic model sliced along the three oriented drill holes north of Lovisa Zn-Pb (section labeled “A” in Fig. 10). Black square outlines area shown in B and C. (B) Lithology and XRF data were used to identify and correlate distinctive Fe-rich marker layers (colored dashed lines) occurring within metamorphosed rhyolitic siltstones. Flat lines in the Fe logs correspond to unscanned sections. (C) Structural measurements interpreted from drill core tomography were used for local refinement of the mesoscopic folding and faulting patterns. Black dashed lines represent form lines, and structural planes ($S_{0,1}$) are shown along drill paths.

(1988). Secondly, the structural measurements from outcrop and drill core 3-D tomography were manually interpolated, revealing a structural pattern dominated by moderately SE-dipping S folds and steeply dipping faults (Fig. 11C). At deeper levels, beyond the extent of drilling, the overall fold geometry of the Guldsmedshyttan syncline was interpreted from 2-D forward modeling of magnetic and gravity data presented in Luth et al. (2019).

At the scale of the Lovisa deposit, an initial Zn-Pb ore shell was modeled in 3-D using lithological and geochemical data from historical drilling and subsurface mapping (Fig. 12A). From the scanned unoriented drill cores intersecting the Zn-Pb ore zones, the orientations of planar and linear features were digitally measured with respect to the core axis and provided useful structural constraints when referenced to the regional trend of the dominant $S_{0,1}$ fabric (e.g., Scott and Berry, 2004). As a result, the boundaries of the main ore, sphalerite ore, and barren interlayers were identified in multiple drill cores, which through drill hole correlation resulted in a refined 3-D geologic model (Fig. 12B). While these major ore zones were already possible to log using conventional methods, the enhanced structural and mineralogical-chemical detail provided by XCT-XRF was particularly useful to distinguish and delineate the finely laminated sphalerite ore, which was previously difficult (cf. Fig. 7H-J).

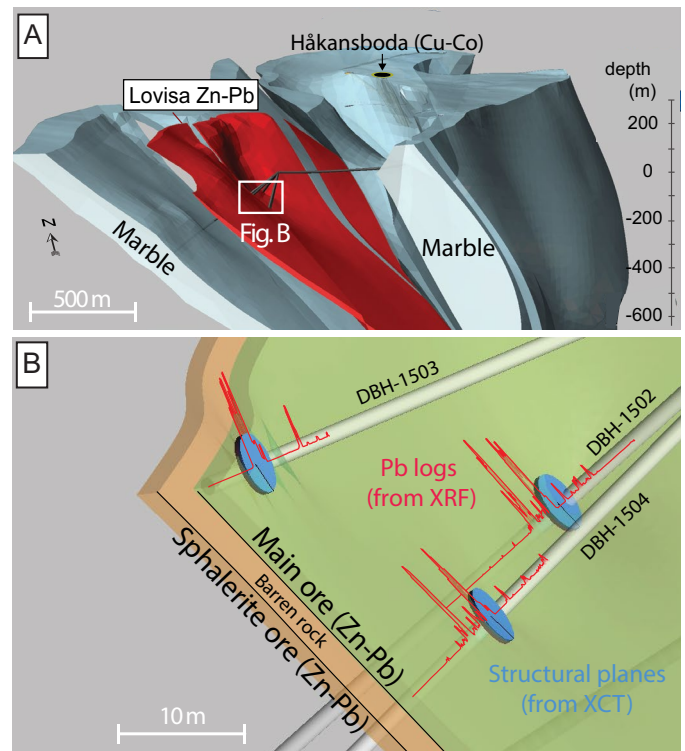


Fig. 12. Integration of X-ray computed tomography and X-ray fluorescence (XCT-XRF) scanning results with 3-D geologic modeling. (A) Initial 3-D ore shell of the Lovisa Zn-Pb deposit (red color) constrained by drilling and underground mapping. Blue color represents marble. Rhyolitic rocks are fully transparent. (B) Part of the refined model based on XCT-XRF scanning data from five drill holes (not all shown) showing the two main ore zones and interlayered barren rock.

Discussion

Structural character of the Lovisa Zn-Pb deposit and its environs

The 3-D model of Lovisa displays a polyphase folding pattern in which NE-striking F_2 folds have been refolded by NW-striking vertical F_3 folds (Fig. 13). This folding pattern is consistent with earlier observations from Carlon and Bleeker (1988), although they interpreted this pattern as due to F_1 - F_2 fold interferences. The difference between the two interpretations arises primarily from the S_0 - S_1 relationship, which in this study was unequivocally determined as consistently parallel planar structures that have been jointly folded by F_2 folds at all scales and locally by F_3 folds.

Deformation history: We propose a fourfold structural history for the Lovisa area comprising three regional deformation phases, commencing with the development of a D_1 planar and linear grain-shape fabric related to tight to isoclinal folding of bedding (F_1 ; e.g., Stålhös, 1981). At Lovisa, determination of D_1 -related fabrics is difficult due to transposition of primary S_0 structures into S_1 followed by recrystallization and finally the transposition of these structures into D_2 - D_3 fabrics.

A second phase of folding and shearing occurred during D_2 under roughly north-south crustal shortening. D_2 deformation

along the West Bergslagen boundary zone is characterized by sinistral transpression producing two distinctive folding patterns, which we interpret as the result of spatial and temporal variability in the degree of strain partitioning. Thus, during early D_2 , N-S-directed crustal shortening was efficiently partitioned along the West Bergslagen boundary zone into contractional domains undergoing isoclinal folding, and a transcurrent component was localized along narrow mylonite zones (D_{2a} in Fig. 13). This stage resulted in the formation of the Guldsmedshyttan syncline with its included pre-tectonic mineralization, which was bounded along its limbs by sinistral mylonite zones to the northwest and southeast. During late D_2 , enhanced mechanical coupling along the West Bergslagen boundary zone and less efficient strain partitioning led to an increased transcurrent component in the contractional domain causing refolding of the isoclinal upright folds along steeply SE-plunging S folds and the development of an L_2 stretching lineation (apparent in most of the XCT-XRF scans; Fig. 6), while the bounding mylonite zones accommodated sinistral-reverse top-to-the-northwest shearing (D_{2b} , Fig. 13). Locally, even the F_2 folds associated with this late D_2 event were refolded as a result of progressive shearing. Finally, crustal shortening became EW-directed during D_3 , causing dextral transpression along the West Bergslagen boundary

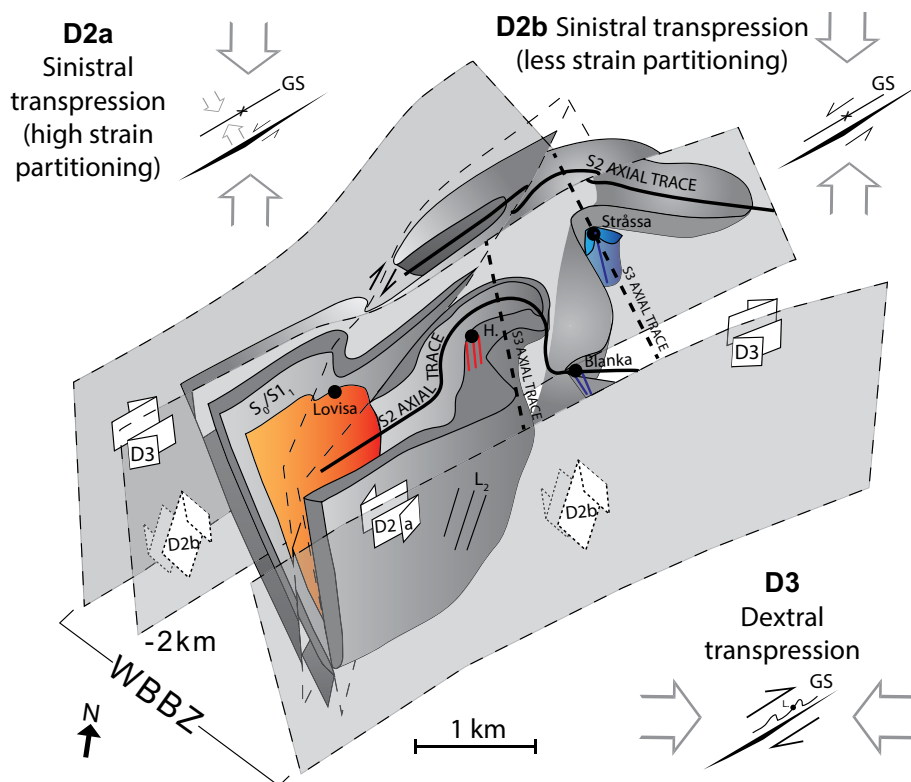


Fig. 13. 3-D cartoon of the interpreted structural setting of the Lovisa Zn-Pb, Håkansboda Cu-Co, Stråssa Fe, and Blanka Fe deposits in relationship to the D_2 - D_3 regional deformation history in Bergslagen. The deposits occur within the refolded northern tip of the Guldsmedshyttan syncline (GS), which is hosted by the West Bergslagen boundary zone (WBBZ). Main cartoon is redrawn from the geologic model displayed in Figure 10. D_2 sinistral transpression along the WBBZ transitioned from a high degree of strain partitioning (D_{2a}), causing upright isoclinal folding and strike slip shearing, toward less efficient strain partitioning (D_{2b}) resulting in oblique folding and shearing. Subsequent D_3 dextral transpression resulted from east-west bulk shortening and was accommodated by drag folding (F_3) at Håkansboda bounded and intersected by discrete dextral strike-slip zones. L_2 represents a penetrative stretching lineation. Inset cartoons are simplified map sketches of the structural setting of the WBBZ and Guldsmedshyttan syncline with hollow arrows indicating the direction of crustal shortening.

zone, which mainly resulted in NW-SE- to N-S-striking vertical F_3 folds with predominantly Z asymmetries, such as at Håkansboda, and dextral shearing along discrete NNW- to NNE-striking mylonite zones.

A consequence of the proposed deformation history outlined above is that there is no need to infer a D_1 deformation phase to have preconditioned vertical F_2 folding by tilting the stratigraphy into a vertical orientation, as proposed by Stålhös (1981) and adapted by Beunk and Kuipers (2012). Instead, all D_2 -related deformation could have been achieved by regional north-south crustal shortening during which the degree of strain partitioning varied with time along the West Bergslagen boundary zone.

Controls on strain partitioning: The degree of strain partitioning depends in part on the rheological weakening along a shear zone (e.g., Mount and Suppe, 1987), which for Lovisa and the West Bergslagen boundary zone in general must have been strongly influenced by the well-stratified supracrustal rocks including sulfide-rich zones and interbedded carbonate, skarn, and chert layers, which strongly contrast with the homogeneous and highly competent intrusive rocks present on either side of the West Bergslagen boundary zone (Fig. 2). Another controlling factor on the degree of strain partitioning is the orientation of the convergence vector relative to the shear zone (e.g., Fossen et al., 1994; Tikoff and Teyssier, 1994), which for the West Bergslagen boundary zone was north-south during D_2 but turned to east-west during D_3 (e.g., Stephens and Jansson, 2020). As a result, D_3 deformation at Lovisa was most likely accommodated by right-lateral displacements and drag folding along the NW-SE-striking shear zones as well as by vertical folding along steeply dipping NNW-SSE-striking axial planes at Håkansboda and Stråssa (Fig. 13). It is plausible that during late D_2 , strain partitioning finally became less efficient as the region evolved from moderately high temperatures to a brittle-ductile regime, leading to enhanced mechanical coupling along the West Bergslagen boundary zone.

Timing of deformation: It is suggested that the proposed D_1 - D_3 progression roughly reflects three tectonic cycles at 1.9–1.76 Ga, which were governed by subduction along a convergent continental margin active in Fennoscandia at that time (e.g., Stephens et al., 2009; Stephens and Jansson, 2020). D_1 -related deformation was preceded by sedimentation, synvolcanic mineralization and magmatism during an early phase of the first tectonic cycle marked by extension caused by a retreating subducting slab at ca. 1.89–1.87 Ga. A switch toward an advancing arc initiated D_1 shortening and M_1 metamorphism during the end of the first and the onset of a second tectonic cycle. Subsequent D_2 shortening and M_2 metamorphism at 1.84–1.82 Ga was probably preceded by another phase of regional extension due to renewed slab retreat (D_3 in Beunk and Kuipers, 2012) causing further magmatism and sedimentation. Beunk and Kuipers (2012) divided D_2 into two stages in which peak M_2 conditions relate to the closure of a back-arc basin, followed by accretion and collision resulting in the formation of the Bergslagen orocline, crustal-scale F_2 folding, and localization of shearing in high-strain zones such as the West Bergslagen boundary zone. Whether the continued magmatism that postdates D_2 marks another phase of crustal extension (e.g., Wahlgren and Stephens, 2020) or resulted from crustal thickening by oroclinal bending (Beunk

and Kuipers, 2012) is uncertain, but the absence of penetrative tectonic fabrics in most of the 1.8–1.76 Ga intrusions, in combination with D_3 kink-like structures and spaced cleavages in the metasupracrustal rocks, suggests that D_3 deformation was local and occurred at relatively low temperatures. The timing of D_3 , however, remains poorly constrained.

Relationships between mineralization and deformation: At Lovisa, the stratiform Zn-Pb sulfide deposit predates D_1 - D_3 deformation and has clearly been affected by folding and shearing. As such, we suggest that the ball ore texture of the main ore developed during D_1 - M_1 and was most likely accentuated during D_2 - M_2 based on the presence of a strong penetrative fabric enclosing internally folded clasts. In line with the interpretation of Jansson et al. (2018), D_2 - D_3 deformation also produced many of the observed parasitic and smaller fold structures affecting the current orebody geometry at Lovisa. Likewise, the overall shape and orientation of the steeply plunging ore shoots at Håkansboda reflect D_2 - D_3 folding and stretching along the SE-dipping shear planes. Within the Håkansboda ore zones, primary depositional and D_1 -related features have been transposed into parallelism, producing pinch-and-swell sulfide bands, breccias, and boudins of banded calc-silicate rocks, all intersected by sulfide vein networks, as noted by Carlson and Bleeker (1988). On a regional scale, steeply plunging ore shoots that developed from originally stratabound massive sulfides are a common feature in Bergslagen—for example, at the Falun Zn-Pb-Cu-(Au-Ag) sulfide deposit (e.g., Kampmann et al., 2016) or at the Garpenberg Zn-Pb-Ag-(Cu-Au) sulfide deposit (Allen et al., 2003; Jansson and Allen, 2011). In general, the high abundance of sulfide mineralization within high-strain zones suggests a strong control by D_2 / D_3 deformation on ore remobilization and vice versa; the presence of sulfide mineralization has likely played a key role in localizing D_2 / D_3 folding and shearing.

Challenges and opportunities for the XCT-XRF scanning technology

For this study, a resolution of 200 μm obtained from scanning 3 m/h appeared sufficient for the identification, characterization, and textural-structural interpretations of ore and host-rock assemblages. However, a challenge for the presented XCT-XRF drill core scanning technique may include the improvement of the tomographic resolution to be able to resolve small grains or mineral inclusions. In theory, a tomographic resolution down to 45 $\mu\text{m}/\text{pixel}$ can already be reached with the GeoCore X10, but this will increase the scanning time significantly. Another challenge is to overcome the problem of overlapping XRF spectral lines, which causes the systematic overestimation of the concentrations of some elements (e.g., Co). A possible solution may be to use other spectral lines, such as Co-K_β , which is only 13.5% of the intrinsic intensity of Co-K_α and demands for separate simulations, calibrations, and measurement routines. Furthermore, a key future development of the XCT-XRF technology and associated processing software should be to allow direct visualization of absolute chemical concentrations and mineralogical composition in 3-D, rather than indirectly by attenuation.

In addition to the above challenges, XCT-XRF scanning adds another step to the core characterization procedure of an exploration or mining operation (see also Cioacă et al.,

2020). However, scanning (1,500 m at 3 m/h) and subsequent digital logging (~25 m/h) of a moderate amount of core at Lovisa has provided a significantly enhanced level of structural and mineralogical-geochemical detail not previously obtainable via conventional methods, thereby allowing for refinement of 3-D geologic models at multiple scales. Some core logging at Lovisa, particularly structural measurements, kinematic indicators, and delineation of the sphalerite ore, was found to be not only more detailed but also considerably faster using the digital XCT-XRF core compared to conventional logging. With continued development, the capabilities and the efficiency of the XCT-XRF scanning technique may increase enough that it could fully substitute some traditional methods. We conclude, however, that the scanning technique at present is best utilized as a complement to conventional methods, where a priori knowledge and validation from the physical core is still needed together with a rigid quality control, enabling detailed, high-quality structural and compositional core logging in 3-D, preferably on well-preserved and oriented drill core (e.g., Kramer Bernhard et al., 2020; Orpen and Orpen, 2020).

Conclusions

It has been demonstrated that combined XCT-XRF drill core scanning is a powerful tool for 3-D rock and ore characterization, generating continuous downhole data sets on structure, texture, mineralogy, chemistry, and density from a single scan. The resulting rotatable 3-D imagery can be shared directly after scanning to allow for joint structural-mineralogical-chemical core logging by (remote) geologists and decision makers, thereby accelerating high-quality 3-D interpretations and multiscale geologic modeling. In its application to the Lovisa stratiform Zn-Pb deposit, XCT-XRF drill core scanning revealed 3-D ore and host-rock textures indicating remobilization of ore minerals and systematic Z and S folding and faulting. With the XCT-XRF-derived information, and in combination with additional geologic and geophysical data, 3-D geologic modeling at Lovisa was refined on multiple scales by adding new structural and chemical constraints to the Zn-Pb ore zones, host-rock units, and regional structural framework. The results indicate a fourfold deformation history at 1.9–1.76 Ga with a strong control exerted by transpressive D₂/D₃ deformation on ore remobilization and orebody geometries at Lovisa and surrounding deposits hosted by the West Bergslagen boundary zone.

Acknowledgments

This study is part of the X-MINE project funded by the European Union's Horizon 2020 research and innovation program under grant agreement 730270. We gratefully acknowledge Ronald Arvidsson, Johan Jönberger, Edine Bakker, Elvís Stansvik, Peter Hedin, Karin Högdahl, and Nils Jansson for their input on various aspects of this study. We thank Michael Gazley, Tobias Bauer, Iain Dalrymple, and the *Economic Geology* Editorial Board for their extensive and constructive reviews of earlier versions of this manuscript.

REFERENCES

Allen, R., Bull, S., Ripa, M., and Jonsson, R., 2003, Regional stratigraphy, basin evolution, and the setting of stratabound Zn-Pb-Cu-Ag-Au deposits in

- Bergslagen, Sweden: Geological Survey of Sweden-Research and Development, Report 03-1203/99, 80 p.
- Allen, R.L., Lundström, I., Ripa, M., and Christofferson, H., 1996, Facies analysis of a 1.9 Ga, continental margin, back-arc, felsic caldera province with diverse Zn-Pb-Ag-(Cu-Au) sulfide and Fe oxide deposits, Bergslagen region, Sweden: *Economic Geology*, v. 91, no. 6, p. 979–1008.
- Bergqvist, M., Landström, E., Hansson, A., and Luth, S., 2019, Access to geological structures, density, minerals and textures through novel combination of 3D tomography, XRF and sample weight: Australian Exploration Geoscience Conference (AEGC), Perth, 2019, Extended Abstracts, v. 1, p. 1–3.
- Beunk, F.F., and Kuipers, G., 2012, The Bergslagen ore province, Sweden: Review and update of an accreted orocline, 1.9–1.8 Ga: *Precambrian Research*, v. 216, p. 95–119.
- Bleeker, W., 1984, Geology of the Stråssa-Torrsvjööboda area and the Håkansboda-Ingelshyttan area, map sheets 11F 4c, 11F 4d, 11F 4e: Exploration report for Luossavaara-Kirunavaara Aktiebolag (LKAB) and British Petroleum (BP) AB Joint Venture, B85-12, 97 p., www.resource.sgu.se/dokument/geodigitalia/rapporter/b_8512.pdf.
- Boas, F., and Fleischman, D., 2011, Evaluation of two iterative techniques for reducing metal artifacts in computed tomography: *Radiology*, v. 259, no. 3, p. 894–902.
- Carlson, C., 1986, Mineralization in the Håkansboda area: Exploration report for Luossavaara-Kirunavaara Aktiebolag (LKAB), B8607, www.resource.sgu.se/dokument/geodigitalia/rapporter/b_8512.pdf.
- Carlson, C., and Bleeker, W., 1988, The geology and structural setting of the Håkansboda Cu-Co-As-Sb-Bi-Au deposit and associated Pb-Zn-Cu-Ag-Sb mineralisation, Bergslagen, central Sweden: *Geologie en Mijnbouw*, v. 67, p. 272–292.
- Carlson, C.J., 1987, The Lovisa project 1985–1986: Exploration report for Luossavaara-Kirunavaara Aktiebolag (LKAB) and British Petroleum (BP) AB Joint Venture, B87-1, v. 1, 127 p., http://resource.sgu.se/dokument/geodigitalia/rapporter/b_8701.pdf.
- Cioacă, M.E., Munteanu, M., Lynch, E.P., Arvanitidis, N., Bergqvist, M., Costin, G., Ivanov, D., Milu, V., Arvidsson, R., Iorga-Pavel, A., Högdahl, K., and Stoilov, V., 2020, Mineralogical setting of precious metals at the Assarel porphyry copper-gold deposit, Bulgaria, as supporting information for the development of new drill core 3D XCT-XRF scanning technology: *Minerals*, v. 10, no. 11, article 946.
- Cnudde, V., and Boone, M.N., 2013, High-resolution X-ray computed tomography in geosciences: A review of the current technology and applications: *Earth-Science Reviews*, v. 123, p. 1–17.
- Dentith, M., Enkin, R.J., Morris, W., Adams, C., and Bourne, B., 2020, Petrophysics and mineral exploration: A workflow for data analysis and a new interpretation framework: *Geophysical Prospecting*, v. 68, p. 178–199.
- Fossen, H., Tikoff, B., and Teyssier, C.T., 1994, Strain modeling of transpressional and transtensional deformation: *Norsk Geologisk Tidsskrift*, v. 74, p. 134–145.
- Gallhofer, D., and Lottermosser, B.G., 2018, The influence of spectral interferences on critical element distributions with portable X-ray fluorescence (pXRF): *Minerals*, v. 8, no. 320, doi: 10.3390/min8080320.
- Geijer, P., 1927, Stråssa och Blanka järnmalmfält: Geological Survey of Sweden, Series Ca 20, 48 p. (in Swedish).
- 1961, The geological significance of the cerium mineral occurrences of the Bastnäs type in central Sweden: *Arkiv för mineralogi och geologi*, v. 3, p. 99–105.
- 1971, Sulfidic “ball ores” and the pebble dikes: Geological Survey of Sweden, Report Series C 662, 29 p.
- Geijer, P., and Magnusson, N.H., 1944, De mellansvenska järnmalmernas geologi: Geological Survey of Sweden, Series Ca 35, 654 p.
- Godel, B., 2013, High-resolution X-ray computed tomography and its application to ore deposits: From data acquisition to quantitative three-dimensional measurements with case studies from Ni-Cu-PGE deposits: *Economic Geology*, v. 108, no. 8, p. 2005–2019.
- Godel, B., Barnes, S.J., and Maier, W.D., 2006, 3-D distribution of sulphide minerals in the Merensky reef (Bushveld Complex, South Africa) and the JM reef (Stillwater Complex, USA) and their relationship to microstructures using X-ray computed tomography: *Journal of Petrology*, v. 47, no. 9, p. 1853–1872.
- Jansson, N.F., and Allen, R.L., 2011, Timing of volcanism, hydrothermal alteration and ore formation at Garpenberg, Bergslagen, Sweden: *GFF, Journal of the Geological Society of Sweden*, v. 133, p. 3–18.

- Jansson, N.F., Sädbom, S., Allen, R.L., Billström, K., and Spry, P.G., 2018, The Lovisa stratiform Zn-Pb deposit, Bergslagen, Sweden: Structure, stratigraphy, and ore genesis: *Economic Geology*, v. 113, no. 3, p. 699–739.
- Jonsson, E., Andersson, S., Sahlström, F., and Högdahl, K., 2020, Sphalerite deformation highlighted by chemical etching and reflected polarised light darkfield and differential interference contrast microscopy: *Nordic Geological Winter Meeting, NGF Oslo, 34th, Oslo, Norway, January 8–10, 2020, Abstracts and Proceedings*, no. 1, p. 107.
- Joseph, P.M., and Spital, R.D., 1982, The effect of scatter in X-ray computed tomography: *Medical Physics*, v. 9, no. 4, p. 464–472.
- Kamb, W.B., 1959, Ice petrofabric observations from Blue Glacier, Washington, in relation to theory and experiment: *Journal of Geophysical Research*, v. 64, no. 11, p. 1891–1909.
- Kampmann, T.C., Stephens, M.B. and Weihed, P., 2016, 3D modeling and sheath folding at the Falun pyritic Zn-Pb-Cu-(Au-Ag) sulphide deposit and implications for exploration in a 1.9 Ga ore district, Fennoscandian Shield, Sweden: *Mineralium Deposita*, v. 51, no. 5, p. 665–680.
- Ketcham, R.A., 2005, Computational methods for quantitative analysis of three-dimensional features in geological specimens: *Geosphere*, v. 1, no. 1, p. 32–41.
- Koark, H., 1960, The geology of the Stråssa, Blanka and Håkansboda districts: XXI International Geological Congress, Grängesbergbolaget, Copenhagen, Denmark, 1960, Proceedings.
- Kramer Bernhard, J., Barnett, W., Uken, R., and Myers, R., 2020, Structural analysis of drill core for mineral exploration and mining: Review and workflow toward domain-based 3D interpretation: *Reviews in Economic Geology*, v. 21, p. 215–245.
- Kruse, F.A., Bedell, R.L., Taranik, J.V., Peppin, W.A., Weatherbee, O., and Calvin, W., 2012, Mapping alteration minerals at prospect, outcrop and drill core scales using imaging spectrometry: *International Journal of Remote Sensing*, v. 33, no. 6, p. 1780–1798.
- Kyle, J.R., and Ketcham, R.A., 2015, Application of high resolution X-ray computed tomography to mineral deposit origin, evaluation, and processing: *Ore Geology Reviews*, v. 65, p. 821–839.
- Kyle, J.R., Mote, A.S., and Ketcham, R.A., 2008, High-resolution X-ray computed tomography studies of Grasberg porphyry Cu-Au ores, Papua, Indonesia: *Mineralium Deposita*, v. 43, no. 5, p. 519–532.
- Laperche, V., and Lemière, B., 2021, Possible pitfalls in the analysis of minerals and loose materials by portable XRF, and how to overcome them: *Minerals*, v. 11, article 33.
- Lovisagruvan AB, 2020, Annual report 2019: www.lovisagruvan.se.
- Lundström, I., 1983, Bedrock map of Lindesberg SV: Geological Survey of Sweden, Series Af 126, scale 1:50,000.
- Luth, S., Sahlström, F., Jansson, N., Jönberger, J., Sädbom, S., Landström, E., Bergqvist, M., Arvanitidis, N., and Arvidsson, R., 2019, Building 3D geo-models using XRF-XRT-generated drillcore data: The Lovisa-Håkansboda base metal-and Stråssa-Blanka iron deposits in Bergslagen, Sweden: Society for Geology Applied to Mineral Deposits (SGA) Biennial Meeting, 15th, Glasgow, 2019, Proceedings, v. 3, p. 1282–1285.
- Mathieu, M., Roy, R., Launeau, P., Cathelineau, M., and Quirt, D., 2017, Alteration mapping on drill cores using a HySpex SWIR-320m hyperspectral camera: Application to the exploration of an unconformity-related uranium deposit (Saskatchewan, Canada): *Journal of Geochemical Exploration*, v. 172, p. 71–88.
- Mount, V.S., and Suppe, J., 1987, State of stress near the San Andreas fault: Implications for wrench tectonics: *Geology*, v. 15, no. 12, p. 1143–1146.
- Mudd, G.M., Jowitt, S.M., and Werner, T.T., 2017, The world's lead-zinc mineral resources: Scarcity, data, issues and opportunities: *Ore Geology Reviews*, v. 80, p. 1160–1190.
- Nassar, N.T., Brainard, J., Gulley, A., Manley, R., Matos, G., Lederer, G., Bird, L.R., Pineault, D., Alonso, E., Gambodi, J., and Fortier, S.M., 2020, Evaluating the mineral commodity supply risk of the US manufacturing sector: *Science Advances*, v. 6, no. 8, doi: 10.1126/sciadv.aay8647.
- Niiranen, T., Nykänen, V., and Lahti, I., 2019, Scalability of the mineral prospectivity modeling—an orogenic gold case study from northern Finland: *Ore Geology Reviews*, v. 109, p. 11–25.
- Orexplore, 2021, <https://orexplore.com>.
- Orpen, J., and Orpen, D., 2020, Error-proofing diamond drilling and drill core measurements: *SEG Discovery*, v. 123, p. 23–34.
- Potts, P.J., and Webb, P.C., 1992, X-ray fluorescence spectrometry: *Geoanalysis*, v. 44, p. 251–296.
- Ryan, C.G., Kirkham, R., Moorhead, G.F., Parry, D., Jensen, M., Faulks, A., Dunn, P., Dodanwala, R., Fisher, L., Pearce, M., Siddons, P., Kuczewski, A., Lundström, U., Trolliet, A., and Gao, N., 2018, Maia Mapper: High definition XRF imaging in the lab: *Journal of Instrumentation*, v. 13, no. 3, article C03020, 8 p.
- Sahlström, F., Jonsson, E., Högdahl, K., Ghaderidosst, J., Luth, S., Lynch, E., Landström, E., and Sädbom, S., 2019a, Textural evolution of the Lovisa Zn-Pb-(Ag) deposit, Bergslagen, Sweden: Insights from microscopy and 3D X-ray tomography: Society for Geology Applied to Mineral Deposits (SGA) Biennial Meeting, 15th, Glasgow, 2019, Proceedings, Proceedings, v. 1, p. 443–446.
- Sahlström, F., Jonsson, E., Högdahl, K., Troll, V.R., Harris, C., Jolis, E.M., and Weis, F., 2019b, Interaction between high-temperature magmatic fluids and limestone explains “Bastnäs-type” REE deposits in central Sweden: *Scientific Reports*, v. 9, no. 1, p. 1–9.
- Salvat, F., Fernandez-Varea, J.M., and Sempau, J., 2006, PENELOPE-2006: A code system for Monte Carlo simulation of electron and photon transport: The OECD Nuclear Energy Agency, PENELOPE-2006 Workshop, Barcelona, July 4–7, 2006, Proceedings, v. 4, no. 6222.
- Scott, R.J., and Berry, R.F., 2004, A new method for obtaining and quantifying the reliability of structural data from axially-oriented drill core using a fabric of known orientation: *Journal of Structural Geology*, v. 26, no. 4, p. 643–658.
- Sjöqvist, A.S.L., Arthursson, M., Lundström, A., Calderon Estrada, E., Inerfeldt, A., and Lorenz, H., 2015, An innovative optical and chemical drill core scanner: *Scientific Drilling*, v. 19, p. 13–15.
- Stålhös, G., 1981, A tectonic model for the Svecokarelian folding in east central Sweden: *Geologiska Föreningen i Stockholm Förhandlingar*, v. 103, no. 1, p. 33–46.
- Stephens, M.B., and Jansson, N.F., 2020, Paleoproterozoic (1.9–1.8 Ga) syn-orogenic magmatism, sedimentation and mineralization in the Bergslagen lithotectonic unit, Svecokarelian orogen: *Geological Society, London, Memoirs*, v. 50, p. 155–206, doi: 10.1144/M50-2018-17.
- Stephens, M.B., Ripa, M., Lundström, I., Persson, L., Bergman, T., Ahl, M., Wahlgren, C.J., Persson, P.O., and Wickström, L., 2009, Synthesis of the bedrock geology in the Bergslagen region, Fennoscandian Shield, south-central Sweden: *Geological Survey of Sweden, Series Ba*, no. 58, 259 p.
- Tegengren, F.R., 1924, Sveriges ädlare malmer och bergverk: *Geological Survey of Sweden, Series Ca 17*, 406 p.
- Tikoff, B., and Teyssier, C., 1994, Strain modeling of displacement-field partitioning in transpressional orogens: *Journal of Structural Geology*, v. 16, no. 11, p. 1575–1588.
- Tonai, S., Kubo, Y., Tsang, M.Y., Bowden, S., Ide, K., Hirose, T., Kamiya, N., Yamamoto, Y., Yang, K., Yamada, Y., Morono, Y., Heuer, V.B., Inagaki, F., and Expedition 370 Scientists, 2019, A new method for quality control of geological cores by X-ray computed tomography: Application in IODP expedition 370: *Frontiers in Earth Science*, v. 7, doi: 10.3389/feart.2019.00117.
- Vokes, F.M., 1969, A review of the metamorphism of sulphide deposit: *Earth-Science Reviews*, v. 5, p. 99–143.
- 1973, “Ball texture” in sulphide ores: *Geologiska Föreningens i Stockholm Förhandlingar*, v. 95, p. 403–406.
- Wahlgren, C.H., and Stephens, M.B., 2020, Småland lithotectonic unit dominated by Paleoproterozoic (1.8 Ga) syn-orogenic magmatism, Svecokarelian orogen: *Geological Society, London, Memoirs*, v. 50, p. 207–235, doi: 10.1144/M50-2017-19.
- Wiedenbeck, M., 2013, The elements toolkit: Field-portable XRF: A geochemist's dream?: *Elements*, v. 9, no. 1, p. 7–8.
- Willemink, M.J., Persson, M., Pourmorteza, A., Pelc, N.J., and Fleischmann, D., 2018, Photon-counting CT: Technical principles and clinical prospects: *Radiology*, v. 289, no. 2, p. 293–312.
- Williams, J.N., Toy, V.G., Massiot, C., McNamara, D.D., Smith, S.A.F., and Mills, S., 2018, Controls on fault zone structure and brittle fracturing in the foliated hanging wall of the Alpine fault: *Solid Earth*, v. 9, p. 469–489, doi: 10.5194/se-9-469-2018.
- Wood, D., and Hedenquist, J., 2019, Mineral exploration: Discovering and defining ore deposits: *SEG Newsletter*, no. 116, p. 11–22, doi: 10.5382/Geo-and-Mining-02.
- Young, K.E., Evans, C.A., Hodges, K.V., Bleacher, J.E., and Graff, T.G., 2016, A review of the handheld X-ray fluorescence spectrometer as a tool for field geologic investigations on Earth and in planetary surface exploration: *Applied Geochemistry*, v. 72, p. 77–87.

Stefan Luth is a structural geologist at the Geological Survey of Sweden, where he combines field work with 3-D geologic and geophysical modeling to construct multiscale 4-D geologic frameworks for ore deposits throughout Sweden and other European countries. In 2011 he obtained his Ph.D. degree at Vrije Universiteit Amsterdam on lithosphere-scale analogue modeling of continental subduction below the Alps. More recently, his research interest focuses on the demonstration and implementation of new geologic and geophysical tools for mapping, 3-D modeling, and mineral exploration.



